Mon. Not. R. Astron. Soc. **000**, 000–000 (0000) Printed 6 May 2015 (MN LATEX style file v2.2)

The Cepheid distance to the maser-host galaxy NGC 4258: Studying systematics with the Large Binocular Telescope

M. M. Fausnaugh,[1] C. S. Kochanek,[1,2] J. R. Gerke,[1]
L. M. Macri,[3] A. G. Riess,[4,5] and K. Z. Stanek[1]
[1]*Department of Astronomy, The Ohio State University, 140 West 18th Avenue, Columbus, OH 43210, USA*
[2]*Center for Cosmology and AstroParticle Physics, The Ohio State University, 191 West Woodruff Avenue, Columbus, OH 43210,USA*
[3]*George P. and Cynthia Woods Mitchell Institute for Fundamental Physics and Astronomy, Department of Physics & Astronomy, Texas A&M University, 4242 TAMU, College Station, TX 77843-4242, USA*
[4]*Department of Physics and Astronomy, Johns Hopkins University, Baltimore, MD 21218, USA*
[5]*Space Telescope Science Institute, 3700 San Martin Drive, Baltimore, MD 21218, USA*

arXiv:1412.2138v2 [astro-ph.GA] 5 May 2015

6 May 2015

ABSTRACT

We identify and phase a sample of 81 Cepheids in the maser-host galaxy NGC 4258 using the Large Binocular Telescope (LBT), and obtain calibrated mean magnitudes in up to 4 filters for a subset of 43 Cepheids using archival *HST* data. We employ 3 models to study the systematic effects of extinction, the assumed extinction law, and metallicity on the Cepheid distance to NGC 4258. We find a correction to the Cepheid colors consistent with a grayer extinction law in NGC 4258 compared to the Milky Way ($R_V = 4.9^{+0.9}_{-0.7}$), although we believe this is indicative of other systematic effects. If we combine our Cepheid sample with previously known Cepheids, we find a significant metallicity adjustment to the distance modulus of $\gamma_1 = -0.61 \pm 0.21$ mag/dex for the Zaritsky et al. (1994) metallicity scale, as well as a weak trend of Cepheid colors with metallicity. Conclusions about the absolute effect of metallicity on Cepheid mean magnitudes are limited by the available data on the metallicity gradient in NGC 4258, but our Cepheid data require at least some metallicity adjustment to make the Cepheid distance consistent with independent distances to the LMC and NGC 4258. From our ensemble of models and the geometric maser distance of NGC 4258 ($\mu_{N4258} = 29.40 \pm 0.06$ mag), we estimate $\mu_{LMC} = 18.57 \pm 0.14$ mag (51.82 ± 3.23 kpc), including the uncertainties due to metallicity.

Key words: stars: variables: Cepheids - galaxies: individual: NGC 4258

1 INTRODUCTION

Cepheid variables remain important for cosmological studies because they anchor the local cosmological distance scale (see the review by Freedman & Madore 2010). Recent measurements of the Hubble constant H_0 from Cepheids (Riess et al. 2011, Freedman et al. 2012, Efstathiou 2014) are in moderate tension with determinations from from the cosmic microwave background (Planck Collaboration et al. 2014) and baryon acoustic oscillations (Anderson et al. 2008). If these discrepancies are confirmed at higher significance, they could be evidence of 'new Physics,' for example, an additional relativistic species in the early Universe. However, before such claims can be made, it is critical to have a better understanding of systematic uncertainties in the local distance scale. These uncertainties include calibration of the Cepheid period-luminosity (PL) relation, and any dependence of the mean magnitudes and colors on extinction, metallicity, and blending.

Determining the absolute zero point of the PL relation requires either a sample of Galactic Cepheids at known distances, or (at least) one independently determined distance to an external galaxy. The Large Magellanic Cloud (LMC), as the closest galaxy to the Milky Way, has traditionally served as the calibrating galaxy (Freedman et al. 2012). Several independent distances to the LMC exist, such as those derived from eclipsing binaries (Bonanos et al. 2011, Pietrzyński et al. 2013) or red-clump stars (Subramanian & Subramaniam 2013). However, uncertainties in the distance to the LMC continue to be a significant source of systematic error for the Cepheid distance scale. Recently, an alternative calibrating galaxy has been provided by NGC 4258. A precise geometric distance to this galaxy (3%) has been determined by Humphreys et al. (2013) based on the kinematics of water masers near the galaxy's nucleus. Such a high precision measurement makes NGC 4258 a good candidate for calibrating the Cepheid PL relation. If NGC 4258 is to serve as the calibrating galaxy, it is extremely important to understand the systematic effects influencing the PL relation and Cepheid mean magnitudes in this galaxy. Moreover, if the independent dis-

© 0000 RAS

tances to the LMC and NGC 4258 are correct, they provide a powerful check on systematic effects in the Cepheid distance scale.

For Cepheids, the standard approach for treating extinction is to obtain two-band photometry, from which it is trivial to estimate an extinction correction given a known extinction law (the so-called "Wesenheit" indices). Recent work has focused on expanding observations of Cepheids to the near and mid-infrared (IR), where the effects of extinction are significantly smaller than in the optical. However, it is usually assumed that the form of the extinction law follows the Cardelli et al. (1989) parameterization, with the ratio of total to selective extinction $R_V = A_V/E(B-V)$ chosen to be either 3.1 or 3.3 (e.g., Macri et al. 2006, Shappee & Stanek 2011, Gerke et al. 2011, Riess et al. 2011, and Freedman et al. 2012). While $R_V = 3.1$ is a reasonable average for sight lines within our own galaxy, it is also known that the extinction law varies between sight lines and galaxies, presumably due to variations in the physical properties of the dust grains (Cardelli et al. 1989). Most Cepheid studies approach this problem by simply adding a small contribution ($\leq 1\%$) to the systematic error budget for the uncertainty in R_V (e.g., Riess et al. 2009 and Shappee & Stanek 2011), although a few studies measure R_V directly or explore its effects on the distance modulus. For example, Pejcha & Kochanek (2012) were able to measure the mean extinction law for a large sample of Cepheids drawn from the Galaxy, LMC, and Small Magellanic Cloud, and they found $R_V = 3.127$, in good agreement with the canonical value. Nevertheless, even in the near and mid-IR, the extinction law exhibits variations of shape along different sight lines (Flaherty et al. 2007, Nishiyama et al. 2009), and it is an open question whether $R_V = 3.1$ is a reasonable estimate of this parameter for all galaxies.

Metallicity is also expected to have an important effect on Cepheid mean magnitudes and colors (e.g., Romaniello et al. 2008, Bono et al. 2010, Freedman & Madore 2011). Studies to date depend on galaxies with significant metallicity gradients, for example M101 (Kennicutt et al. 1998 and Shappee & Stanek 2011) or M81 (Gerke et al. 2011), but the gradients (and hence the impact of metallicity on Cepheid distances) depend sensitively on the method used to measure the metallicity of H II regions in the host galaxy (e.g., Bresolin 2011ab). Previous empirical measurements of the metallicity effect on distances have ranged from non-detections to -0.89 mag/dex, with typical values of about -0.27 mag/dex. The general consensus is that metal-rich Cepheids are brighter and redder than their metal-poor counterparts (Gould 1994, Kochanek 1997, Kennicutt et al. 1998, Macri et al. 2006, Shappee & Stanek 2011, Gerke et al. 2011, Mager et al. 2013). Furthermore, stellar pulsation models indicate that the metallicity dependence varies across pass bands, and may not be a monotonic function of wavelength (Bono et al. 2008, Bono et al. 2010). Improvements in our understanding of the metallicity effect require data to be gathered in a wide range of photometric bands, as well as obtaining better estimates of Cepheid metallicities or their proxies.

Finally, Cepheid mean magnitudes may be biased due to blending (Stanek & Udalski 1999, Mochejska et al. 2000, Macri et al. 2001, Chavez et al. 2012). As massive stars, a sizable fraction of Cepheids are expected to have nearby unresolved companions, which will bias the Cepheid mean magnitudes, reduce their apparent amplitudes, and (typically) make them appear bluer. The effects of blending have been estimated by injecting artificial stars into the PSF of known Cepheids, and looking for changes in the recovered photometry (e.g., Riess et al. 2009, Riess et al. 2011). However, no study has systematically determined the magnitude of this effect, particularly as a function of distance, and existing corrections do not take into account the strong clustering of massive stars (Harris & Zaritsky 1999).

In this study, we redetermine the Cepheid distance to NGC 4258 and examine the effects of extinction, the assumed extinction law, and metallicity on the measured distance. The last independent selection of a Cepheid sample in NGC 4258 was by Macri et al. (2006, hereafter M06). Their large Cepheid sample (89 Cepheids were used in the final fit) was identified with the *Hubble Space Telescope* (*HST*) in two fields at different galactocentric radii – an "inner" field at 6.3 kpc and "outer" field at 17.1 kpc. They found a distance modulus relative to the LMC of $10.71 \pm 0.04_{stat} \pm 0.05_{sys}$ mag for the inner field and $10.87 \pm 0.05_{stat} \pm 0.05_{sys}$ mag for the outer field. Based on the metallicity gradient determined by Zaritsky et al. (1994, hereafter Z94), they interpreted this difference as a metallicity effect, with a dependence of $-0.29 \pm 0.09_{stat} \pm 0.05_{sys}$ mag/dex.

Here, we identify a new Cepheid sample in NGC 4258, drawn from a wide range of galactocentric radii and azimuthal angles using the Large Binocular Telescope (LBT), and calibrate the Cepheid mean magnitudes in four bands using *HST*. In §2 we describe our observations, period search, and criteria for identifying Cepheids. In §3 we explain our procedure for calibrating the Cepheid mean magnitudes from *HST* observations. In §4 we describe three models for the distance to NGC 4258, in which we sequentially explore the effects of extinction, the assumed extinction law, and metallicity on the estimated distance modulus. In §5, we present our results and compare them to previous studies. Finally, in §6, we review the systematic effects associated with this study, and provide a calibration of the absolute PL relations.

2 OBSERVATIONS AND DATA REDUCTION

NGC 4258 was observed on 32 nights between March of 2008 and June of 2013 with the Large Binocular Cameras (LBC, Giallongo et al. 2008) on the LBT (Hill et al. 2010), as part of an observational search for failed supernovae (Gerke et al. 2014). Each camera has an approximate field of view of $23'$x$23'$, easily framing the entire disk of NGC 4258. The LBC consists of 2 cameras, one for each primary mirror, with LBC/Blue optimized for wavelengths of 320-500 nm, and LBC/Red for wavelengths of 500-1000 nm. Four to nine exposures were obtained each night, each of 200 seconds. The blue-side observations cycled through the UBV filters, while the red side only used the R band. Images were over-scan corrected, bias subtracted, and flat fielded using the IRAF MSCRED package. The nightly exposures were then averaged into a single image, or averaged into 2 images if more than 8 exposures were available. These procedures yielded 32–35 images in each of the Johnson/Cousins $UBVR$ bands. After excluding images where the full width at half the maximum (FWHM) of the point spread function (PSF) exceeded $1\farcs6$, we were left with 20–26 images per filter.

Following Gerke et al. (2011, hereafter G11), we searched for variable sources using the ISIS image subtraction package (Alard & Lupton 1998). We first built a reference image from the 4–5 images with the best seeing and lowest sky levels in all filters. All images were then registered and aligned to the frame of the R band reference image. The reference image was scaled and convolved with a spatially variable kernel to match the PSF for each epoch, and then subtracted to leave only sources with variable flux. We next constructed a "variability" image, equal to the root-mean-square (rms) of the subtracted images, and identified variable sources using Sextractor (Bertin & Arnouts 1996). This procedure yielded

approximately 2000 variable sources in each band. We extracted lightcurves for these sources using ISIS's photometry package.

2.1 Period search

In order to identify Cepheid variables, we adopted the Cepheid lightcurve templates constructed by Pejcha & Kochanek (2012), and employed a brute force fitting routine. These templates have the virtues of being physically motivated and derived from a large data set–177,314 data points from 287 Cepheids in 29 different bands. The templates parameterize a Cepheid lightcurve as variation in the star's temperature and radius. The time dependence is modeled by a 20-term Fourier series, and the flux in a given filter is calculated directly from the physical parameters. We used the resulting template lightcurves[1] $T_F(\phi)$ for filter F at phase ϕ, each with self-consistently scaled amplitudes for fundamental mode Cepheids with periods P between 10 and 100 days. We restricted our Cepheid sample to the same range of periods, fitting the lightcurves to the templates by phasing the data to 415 different periods between 10 and 100 days. This has no practical consequences, since $P \leq 10$ day Cepheids are too faint for the LBT survey and $P > 100$ day Cepheids are both rare and likely to lie on a different PL relation (Bird et al. 2009). The phase at an epoch t_i

$$\phi_i = \frac{t_i - t_0}{P} \tag{1}$$

is determined by the period P and a reference time t_0. The periods were chosen so that the phase shift between sequential periods over the span of the data ($\Delta t = 1919.8$ days, about 5 years) was

$$\delta\phi = -\frac{\Delta t}{P^2}\delta P = 0.4 \text{ radians}. \tag{2}$$

The value of 0.4 radians (6% of a full cycle) was empirically tested by applying the method to the known Cepheids in M81 from G11.

For each LBT B, V, and R band lightcurve, we converted the differential counts and their uncertainties to fiducial magnitudes arbitrarily centered at 13.5 mag (the calibration of the mean magnitudes is discussed in §3), and fit the observed lightcurves to the templates by minimizing

$$\chi^2 = \sum_i \left(\frac{m_{Fi} - (\hat{m} + AT_F(\phi_i))}{\sigma_i} \right)^2 \tag{3}$$

where $\hat{m}$ and A are the mean magnitude and the amplitude of the Cepheid model, and σ_i is is the uncertainty in the measurement. We made no attempt to match lightcurves in the three different bands until after the period search, so as to impose an additional check on our procedure. Using an implementation of the Levenberg-Marquardt χ^2–minimization algorithm (MPFIT, Markwardt 2009), we allowed $\hat{m}$, A, and t_0 to freely vary and calculated the minimum χ^2 for our grid of periods. We then sampled an additional 100 periods spanning the interval around the best-fit period. The period with the over-all minimum value of χ^2 was taken as an initial estimate. This approach has the advantage over periodograms of using the period-dependent shape of the lightcurve to help break period degeneracies (aliases).

To eliminate variables that are not Cepheids, we first compared each source's goodness of fit as a Cepheid, χ^2_C, to that for a linear trend, χ^2_{lin}, using the F-test. The F statistic is defined as

$$F = \frac{\chi^2_{\rm lin}/dof}{\chi^2_{\rm C}/dof}, \tag{4}$$

where dof is the number of degrees of freedom in the fit. We eliminated all light curves with $F < 2.5$ from our sample—for Gaussian statistics, with $F > 2.5$ and $dof \sim 25$ (depending on the fit, the lightcurve, and the filter), the hypothesis that both models fit the data equally well can be ruled out at $> 99\%$ confidence. In practice, we only use this cut to reduce the number of candidates, since contaminants such as single epoch novae also pass the F test. This left us with 156 lightcurves to examine by eye, both for the quality of the fits and for any obvious problems in the subtracted images. After verifying that the lightcurves followed the typical saw-tooth pattern characteristic of longer-period Cepheid variables, and that all objects had clean subtractions, we matched lightcurves extracted from different filters by spatial coordinates. This allows us to check the recovered periods of unique Cepheids in different filters. Our procedure yielded 81 unique Cepheids, 40 of which were matched in two or more filters. We found the periods from different filters to be in excellent agreement – the average difference in period was 0.005 days. The coordinates and periods of the Cepheids are reported in Tables 1 and 2.

An additional complication arose from the systematic underestimation of lightcurve uncertainties by ISIS. This underestimation does not affect the F-test because the F-test only compares the relative ability of two models to describe a given data set. However, for our determination of the mean magnitudes (§3), it is useful to adjust the formal errorbars so that they are consistent with the observed scatter. The retained lightcurves typically had formal χ^2_C/dof values of $1.2 - 9.7$, with a median value of 4.0. Three of the brightest Cepheids had χ^2_C/dof greater than 10.0, with the maximum being 22.1, due to the small fractional uncertainty estimates of ISIS. In all cases, we broadened the photometric uncertainties so that $\chi^2_C/dof = 1$ for each individual lightcurve.

3 HST CALIBRATION

The next step is to measure the Cepheid's apparent magnitudes and determine the true value of $\hat{m}$. However, photometric measurements in the LBT reference images are subject to considerable uncertainty due to crowding and confusion with other sources. Instead, we calibrate the Cepheid lightcurves and determine $\hat{m}$ from higher-resolution *HST* data. NGC 4258 was observed as part of the Supernovae and H_0 for the Equation of State (SH0ES) project (Riess et al. 2009). There were 17 observations of NGC 4258 between December of 2009 and May of 2010 using the Advanced Camera for Surveys (ACS) and Wide Field Camera 3 (WFC3) in the F435W, F555W, F814W, and F160W filters. These filters roughly correspond to the Johnson/Cousins $BVIH$ bands, and the observations spanned most of the galaxy's disk. PSF photometry was performed on the images, with fluxes calculated in the *HST* VEGAMAG system. A full description of the data reduction and PSF photometry procedures can be found in Riess et al. (2009) and Riess et al. (2011).

The LBT Cepheid candidates were matched with *HST* sources by calculating the mean offsets of the brightest stars in the *HST* F555W images from the LBT V band images, and shifting all LBT sources by this amount. Any *HST* source within $0\farcs23$ (~ 1 LBC pixel) was selected as a potential match. All matches were verified by eye, and sources that lacked clean, isolated matches were

[1] The templates can be downloaded at `http://www.astronomy.ohio-state.edu/~pejcha/cepheids/` and are available as tables in Pejcha & Kochanek (2012).

cut from our sample. In practice, the mean shifts were less than $0\farcs05$. A few sources were cut due to crowded/confused matches, but roughly a quarter of our sample did not match any bright *HST* sources. It is likely that these sources lacked sufficient contrast with the galaxy's surface brightness to be identified in the *HST* images, even though we detected them in the subtracted LBT images. While *HST* provides less crowded direct images, the LBT variability image is even less crowded, allowing the robust identification of variables even in very dense stellar fields. An additional check was made on the photometric sharpness of each source. Anomalously high or low sharpness measurements indicate blends, extended sources, or image processing artifacts (cosmic rays, etc.). All sources met our sharpness criterion of $-1 \leq S \leq 1$.

Of our 81 Cepheid candidates, 16 were outside of the *HST* footprint. Of the remaining 65, we found 49 unambiguous matches in the *HST* fields. Through this point, each Cepheid had some mixture of B, V, and R band LBT lightcurves. However, we required B and V band LBT lightcurves for our calibration procedure. If either lightcurve was missing from the LBT data, we forced ISIS to extract photometry at the position of the source in the subtracted LBT images for the missing filter, and visually inspected the phased lightcurves. This step was necessary for 20 sources, which were primarily missing B band lightcurves. Six sources were rejected because the newly extracted lightcurves were poorly phased, bringing our sample to 43 Cepheids. We then re-scaled the lightcurve uncertainties as described above.

We next attempted to identify these sources in the *HST* F160W filter images. Sources in the BVI images do not always have obvious near IR counterparts (Riess et al. 2011), and the footprint of the F160W band is not identical to that of the optical data. We extracted F160W band photometry for the expected position of the Cepheids based on their F555W band positions. Of our *HST*-matched sample, 11 Cepheids were outside of the *HST* F160W band coverage of NGC 4258. For 8 other Cepheids, the F160W band measurements were unreliable, with uncertainties > 1.0 magnitudes. Our final *HST*-calibrated sample consists of 43 Cepheids, 24 of which have usable $BVIH$ photometry, 17 have BVI photometry, and 2 Cepheids only have VI photometry.

3.1 Calibration

We do not want to simply use the *HST* magnitudes as a random phase estimate of $\hat{m}$. Rather, we use the LBT data and the Pejcha & Kochanek (2012) templates described in §2.1 to determine the phases and amplitudes of the Cepheids at each epoch of the *HST* observations. At the time of the *HST* observation, the observed magnitude in a filter F is given by

$$m_F = \hat{m}_F + A_F T_F(\phi_{HST} - \phi_0). \tag{5}$$

where T_F is the same template defined in §2.1. With knowledge of the amplitude and the phase, we can determine the mean magnitude $\hat{m}_F$ by fitting m_F to the observed *HST* data. The phase difference $\phi_{HST} - \phi_0 = (t_{HST} - t_0)/P$ is defined by the phase ϕ_0 at the time of the first LBT observation t_0, as compared to the time of the *HST* observation t_{HST}. Since the epochs of the LBT and *HST* data overlap, there is little ambiguity about the relative phasing.

To accurately determine A_F and ϕ_0, we model the LBT differential lightcurves by recasting the flux of the template lightcurves in terms of differential counts

$$\Delta C_{Fi} = 10^{-0.4(\hat{m}_F + A_F T_F(\phi_i - \phi_0) - Z_F)} - C_{0F} \tag{6}$$

where ΔC_{Fi} is the differential counts measured by the LBT in filter F at phase $\phi_i - \phi_0$, C_{0F} is the (unknown) counts of the Cepheid in the LBT reference image of filter F, and Z_F is the photometric zeropoint of the LBT reference image. As a reminder, C_{0F} cannot be reliably determined from the LBT data alone, due to crowding, which is why make use of higher resolution HST data. We determined all of the parameters by optimizing

$$\chi^2 = \sum_F \sum_i \left(\frac{\Delta C_{Fi}^{LBT} - \Delta C_{Fi}}{\sigma_{Fi}^{LBT}} \right)^2 + \sum_F \sum_j \left(\frac{m_{Fj}^{HST} - m_{Fj}}{\sigma_{Fj}^{HST}} \right)^2 \tag{7}$$

where i runs over the LBT observations and j runs over the *HST* observations. The problem is to simultaneously fit for $\hat{m}_F$, A_F, C_{0F}, and ϕ_0. Given the non-linear nature of this task, we performed the calculation using Markov Chain Monte Carlo methods, and estimated the parameter uncertainties from the marginal distributions. We simultaneously fit the B and V band LBT lightcurves and all available *HST* F435W and F555W observations. Given the amplitudes estimated from the data for the V and B bands, the Pejcha & Kochanek (2012) templates determine the amplitudes and phases for all other wavelengths, allowing us to determine $\hat{m}$ for the F814W and F160W bands as well.

The photometric zeropoints Z_F of the LBT reference images were calculated in four steps. First, we found instrumental magnitudes in the reference image using DAOPHOT. Next, we matched the brightest stars in the reference image to SDSS DR7 (Abazajian et al. 2009). We then solved for the zeropoints Z_F that placed our instrumental magnitudes on the Johnson UBV system, following the transformations given by Fukugita et al. (1996). In all, about 60 stars were used to calculate the zeropoints. Finally, the zeropoints were shifted to the *HST* VEGAMAG system, following the zeropoint offsets provided by Sirianni et al. (2005). After accounting for the uncertainties in each transform, we estimate a 0.07 mag error on Z_F in each reference image. However, because we must solve for C_0, the LBT zeropoints only weakly affect the magnitude calibration. G11 found that shifting the zeropoint by as much as 0.30 mag had little effect on the mean magnitudes, changing the final determination of the distance modulus by no more than 0.01 mag. Instead, Z_F primarily influences the determination of the amplitude A, since these parameters are correlated (see G11). However, we usually have 2-3 *HST* calibrating points at differing phases, which helps to constrain the amplitudes and minimizes this problem.

After fitting for the mean magnitudes, we visually checked the calibrated lightcurves and the posterior distributions of their parameters to ensure that the fits had converged and that the parameter space was well-sampled. Because the Cepheids have been calibrated to the *HST* VEGAMAG system, we then converted their mean magnitudes to the Johnson/Cousins BVI system, again following the prescription of Sirianni et al. (2005). These authors determined empirical conversions for *HST* VEGAMAG/Johnson UBV using a zeropoint correction and a single color term. Coefficients for the zeropoint and color term were taken from their Table 18. The typical uncertainty of these transforms is ≤ 0.03 mag, which makes a small contribution to the final calibration uncertainty, typically 0.06–0.10 mag. As already noted, the F160W filter is similar to H band, and we leave these measurements in the native *HST* filter/detector photometric system. Table 1 gives the calibrated mean magnitudes of the Cepheids (with uncertainties including those of the final photometric transform), and Figure 1 provides examples of calibrated B and V band LBT lightcurves.

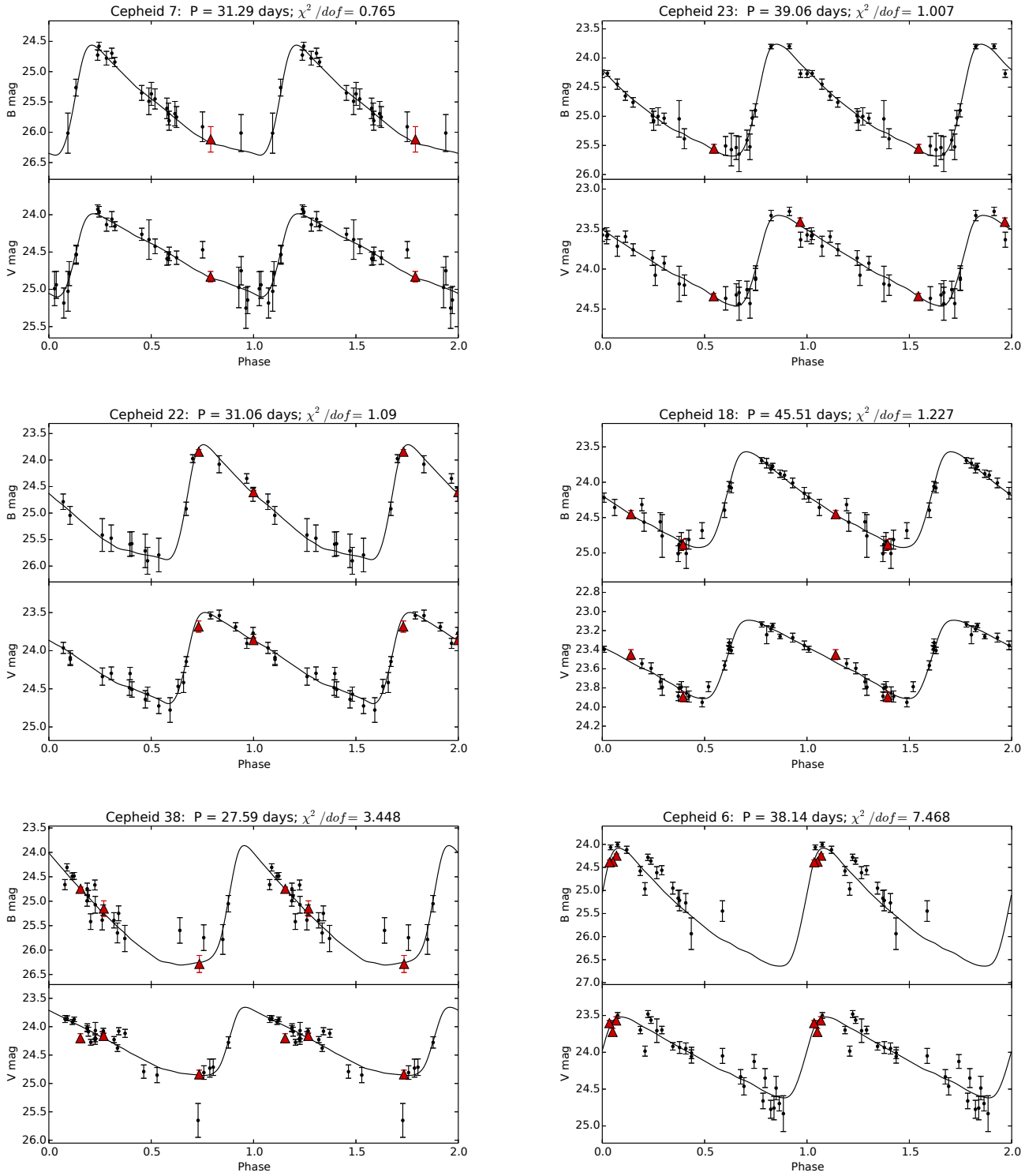
Cepheid 7: P = 31.29 days; $\chi^2/dof=$ 0.765
Cepheid 23: P = 39.06 days; $\chi^2/dof=$ 1.007
Cepheid 22: P = 31.06 days; $\chi^2/dof=$ 1.09
Cepheid 18: P = 45.51 days; $\chi^2/dof=$ 1.227
Cepheid 38: P = 27.59 days; $\chi^2/dof=$ 3.448
Cepheid 6: P = 38.14 days; $\chi^2/dof=$ 7.468
B mag
V mag
Phase

Figure 1. Examples of calibrated lightcurves and their fitted templates. The large red triangles are the *HST* calibration points and the smooth black lines are the empirical templates. The fits degrade from left to right and top to bottom based on the value of χ^2/dof. Cepheid 7 has the smallest value of χ^2/dof among all Cepheids, while Cepheids 38 and 6 have the largest two values.

3.2 Comparison to previous studies

M06 identified a large sample of generally shorter period Cepheids in NGC 4258. The left panel of Figure 2 compares the raw PL relations for the two samples, with no corrections for extinction. Our Cepheids are systematically brighter at fixed period, with average shifts of -0.155 ± 0.011 mag, -0.130 ± 0.007 mag, and -0.061 ± 0.010 mag in the B, V, and I bands. We also compared only those Cepheids in the M06 sample with periods $P > 10$ days, so as to match the range of periods between the two samples. This criterion removed 12 short-period Cepheids from the M06 sample, and increased the mean offset between samples to -0.209 mag, -0.139 mag, and -0.063 mag in B, V, and I, respectively. However, our sample is drawn from a much larger extent of the galaxy's disk, and we might reasonably expect a smaller mean value of extinction. To test this hypothesis, we selected the subset of our Cepheid sample interior to the outer edge of M06 inner field, and we found smaller offsets of -0.099 ± 0.02 mag, -0.003 ± 0.014 mag, and -0.050 ± 0.017 mag in the B, V, and I bands, respectively, shown in the right panel of Figure 2. The dispersions of both samples (the LBT Cepheids and all M06 Cepheids) around their PL relations are almost identical at 0.36 mag, 0.30 mag, and 0.23 mag for the B, V, and I bands.

We can also compare individual Cepheids between samples. We matched seven Cepheids from the M06 sample in the LBT sample, and compared the periods and mean magnitudes. The limited overlap comes from the difference in period ranges (see Figure 2). As an experiment, we examined the positions of the M06 Cepheids in our rms image by eye. We found two additional Cepheids that matched sources for which we had extracted lightcurves. One Cepheid was not identified because it had a period of 8.96 days, and was therefore excluded from our period search. The other M06 Cepheid had a period of 32.25 days and was identified in the LBT R band with $F = 3.59$ and a period of 32.85 days. However, it was cut during our visual inspection step because of a particularly small amplitude (0.02 mag) compared to its scatter. The original *HST* light curve from M06 has an amplitude of 1.2 mag, suggesting that the image subtractions and extracted photometry for this source are particularly noisy.

Table 3 summarizes the differences in period and mean magnitudes for the seven matches. The agreement of the periods is good, with typical differences of a few tenths of a day. The M06 observations spanned $\Delta t = 45$ days, so we would not expect periods more accurate than $\delta P = 0.4P^2/\Delta t \sim 0.9(P/10 \text{ days})^2$ days. The average absolute shift is 0.58 days. Two Cepheids had $\Delta P > 1$ days, and these were the two with the longest periods (26.99 and 36.95 days). Our mean magnitudes tend to be fainter than those of M06, although the average differences are comparable to their dispersion. Two Cepheids had differences in two or more filters greater than 0.20 magnitudes. Cepheid 39 is near the galaxy's center, while Cepheid 31 is one of our faintest Cepheids. Figure 3 displays the LBT lightcurves of these Cepheids, overlaid with the M06 lightcurves shifted to a common phase. For comparison, the Cepheid with the smallest difference in mean magnitudes (Cepheid 40) is also shown. The *HST* calibration points are clearly offset from the M06 lightcurves for Cepheid 39, and there is some suggestion of the same effect in the V band for Cepheid 31. The mean magnitudes from M06 were calculated by numerically integrating the Stetson (1996) Cepheid lightcurve templates to find the phase-weighted mean magnitude, which may result in small offsets from the mean magnitudes determined in our fitting procedure. If we exclude these 2 Cepheids, the average differences between the mean magnitudes drop to -0.02 ± 0.08 mag, -0.05 ± 0.04 mag, and -0.08 ± 0.07 mag in B, V, and I.

4 DISTANCE FITTING PROCEDURE AND PL RELATIONS

We model the mean magnitude of Cepheid i in filter F as

$$\langle m \rangle_{iF}^{PL} = L_F(P_i) + E_i(B-V)R_F + \boldsymbol{\gamma}(Z_i - Z_{LMC}) + \Delta\mu_{LMC} \quad (8)$$

where $L_F(P_i) = a_F + b_F \log P_i$ is the LMC PL relation, $E_i(B-V)$ is the unique reddening for each Cepheid, $R_F = A_{iF}/E_i(B-V)$ is determined by the extinction law, $Z_i - Z_{LMC}$ is the metallicity of the Cepheid relative to the LMC, $\boldsymbol{\gamma}$ is the metallicity effect (the structure of $\boldsymbol{\gamma}$ is discussed in §5.2), and $\Delta\mu_{LMC}$ is the distance modulus between NGC 4258 and the LMC. Our strategy is to solve for the $E_i(B-V)$, $\boldsymbol{\gamma}$, and $\Delta\mu_{LMC}$ by minimizing the function

$$\chi^2 = \sum_i \sum_F \left(\frac{\hat{m}_{Fi} - \langle m \rangle_{Fi}^{PL}}{\sigma_{Fi}} \right)^2 . \quad (9)$$

We fit all the mean magnitude data simultaneously. However, only $\sim 50\%$ of our sample has complete 4-band photometry. Missing measurements for any filter were assigned a mean magnitude corresponding to the Cepheid lying on the relevant PL relation at the M06 distance modulus. An uncertainty of $\sigma_{Fi} = 10^6$ mag was assigned to this value so that it makes no contribution to the likelihood, while simplifying the 'bookkeeping' of the fit. When we account for the number of degrees of freedom in the model, we do not include these dummy measurements, nor do we incorporate them in our calculation of the covariances between residuals in different filters. In addition to comparing the results of the LBT Cepheid sample to those of M06, we combine both data sets, fitting all 122 Cepheids simultaneously.

The standard error on one parameter is the point where $\Delta\chi^2 = 1$. However, the PL relations have intrinsic scatter due to the finite width of the instability strip, which our model must account for. While intrinsic scatter can bias parameter estimates (Weiner et al. 2006, Kelly 2007), the effect, by definition, decreases with sample size. Since we are primarily concerned with estimating $\Delta\mu$ and $\boldsymbol{\gamma}$, our sample size is reasonably large, and the intrinsic scatter is of minimal interest, we treat this problem by simply rescaling the mean magnitude uncertainties so that $\chi^2/dof = 1$. The rescaling factor propagates directly to the parameter uncertainties, and ensures that the fits are consistent with the scatter. To make sure that this method does not mask any other systematic effects, we check these estimates by bootstrap resampling the Cepheids over 10^4 trials, and reporting the median and the symmetric 68% confidence intervals of the distribution. In practice, we found that the bootstrapping uncertainty estimates are consistent with estimates based on $\Delta\chi^2$.

We take PL relations from three sources. First, the Optical Gravitational Lensing Experiment (OGLE) has been monitoring the LMC for over 20 years and has published several iterations of LMC PL relations. OGLE II published PL relations in BVI (Udalski et al. 1999).[2] More recently, Ngeow et al. (2009) matched

[2] We employ the updated coefficients, which can be found at `ftp://sirius.astrouw.edu.pl/ogle/ogle2/varstars/lmc/cep/catalog/README.PL`

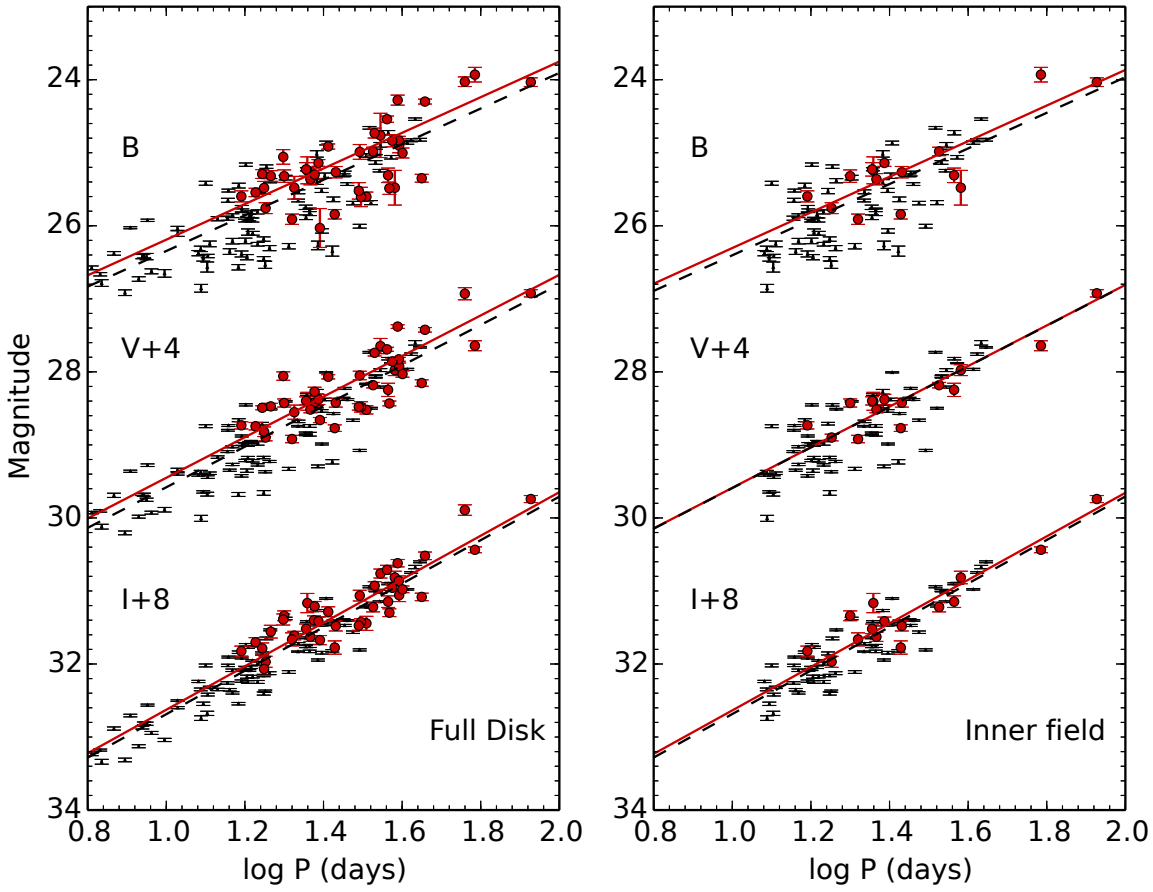

Figure 2. Mean magnitude BVI PL relations for NGC 4258 with no extinction corrections. The large red circles are the LBT Cepheids, and the small points are the Cepheids from M06. The solid lines are the PL relations from M06 shifted to best fit the LBT data, and the dashed lines are the same for the M06 sample. The left panel shows all Cepheids, while the right panel only shows Cepheids interior to the radius of the outer edge of the M06 inner field. The V band and I band results are shifted by 4 and 8 mag, respectively, to avoid overlapping the data.

OGLE III fundamental mode Cepheids to 2MASS data, and published PL relations in $VIJHK$, as well as several Spitzer bands. Both samples were quite large (over 1300 Cepheids). In addition, Persson et al. (2004) determined near-IR PL relations (JHK) using 92 Cepheids. Table 4 summarizes these PL relations. All PL relations have been extinction corrected, and while the various models are nearly consistent, there is some tension. In particular, the I band PL relations from OGLE II and Ngeow et al. (2009) are discrepant at the 3σ level, which Ngeow et al. (2009) attributed to different treatments of extinction. To characterize the dependence of our results on the PL relations, we tested various combinations of these models.

Several studies also suggest that there may be a "break" in the PL relations at ~ 10 days, so that shorter-period Cepheids follow a different PL relation than Cepheids with $P > 10$ days (e.g. Sandage et al. 2004; Kanbur & Ngeow 2004; Ngeow et al. 2009). Since our sample is restricted to longer-period Cepheids, the functional form of the PL relation does not affect our fitting procedure. However, it is possible that modified PL relations derived from long period Cepheids are more appropriate for our sample. We therefore also experimented with the the PL relations of LMC Cepheids with $P > 10$ days, determined by Sandage et al. (2004) and Ngeow et al. (2009).

A complication for our choice of near-IR PL relations is that the *HST* F160W filter/detector combination has an effective wavelength of $\sim 1.5\mu$m, slightly offset from that of H band at $\sim 1.6\mu$m. This calls for a modification to the published near IR PL relation. Near the J and H bands, linear interpolation as a function of wavelength should yield a reasonable estimation of intermediate wavelength PL relations, as shown by Pejcha & Kochanek (2012, see their equation 10 and figure 7). Table 4 includes this modification to the near-IR PL relations, and the errors reported there are determined by adding the errors of the J band and H band PL coefficients in quadrature. This is actually an over-estimate of the uncertainty, since the F160W effective wavelength is ~ 3 times closer to the H band than J band filter, which implies that $\sigma^2_{\rm F160W} = (0.25\sigma_J)^2 + (0.75\sigma_H)^2$. However, we have used the more conservative over-estimate, particularly since it is still much smaller than the intrinsic scatter of the PL relations. In order to further explore the interpolation uncertainty, we modified the F160W PL relation during our bootstrap resampling routine, allowing the interpolated slope and zeropoint to vary by random Gaussian devi-

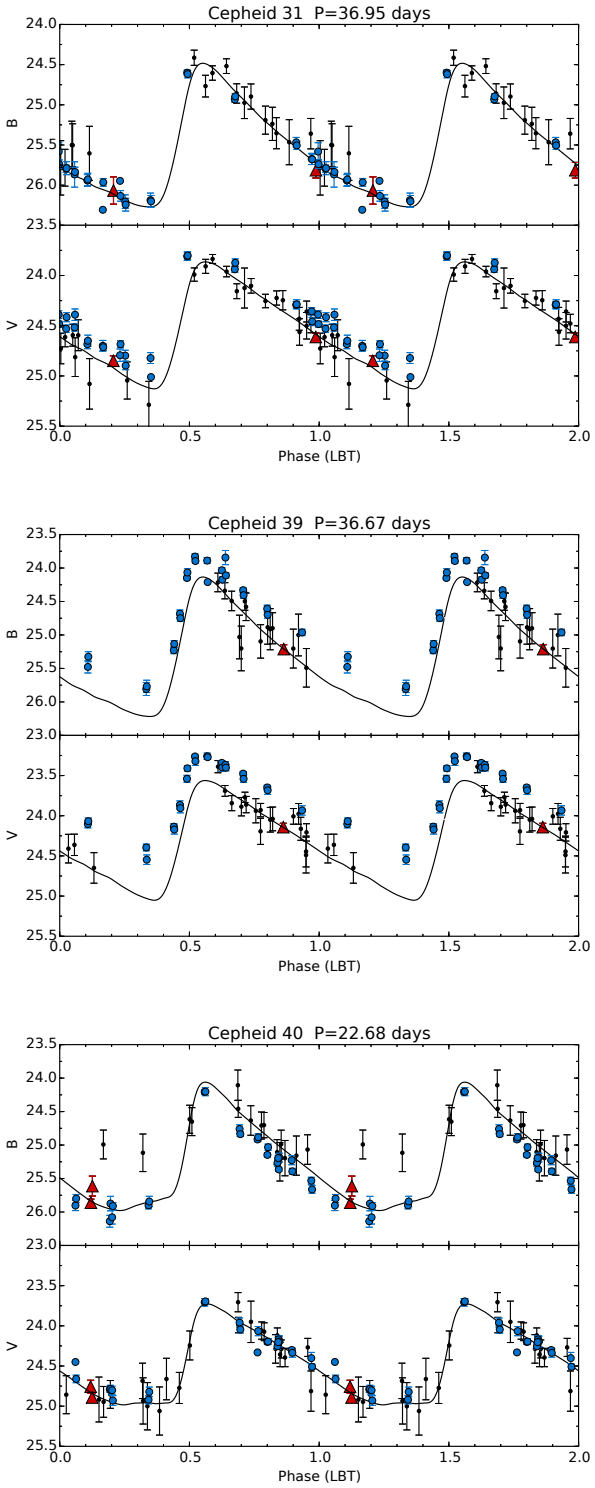

Figure 3. B and V band LBT and M06 lightcurves for the two Cepheids with the largest mean magnitude differences (Cepheids 31, top, and 39, middle) and the smallest difference (Cepheid 40, bottom). The LBT data, with errors, and fitted Pejcha & Kochanek (2012) templates are in black, while the *HST* calibration points are the red triangles. The M06 data are the larger blue circles.

ates scaled by the errors in Table 4. This method samples a range of PL relations intermediate between the J and H bands—in fact, inspection of Table 4 indicates that the P04 PL relations are consistent within 1 to 2.3σ, so this procedure effectively includes the uncertainties of using either the J or H band PL relations themselves.

We adopt a Cardelli et al. (1989) extinction law to set the ratio of total to selective extinction in each band, $R_F = A_F/E(B-V)$. For our first estimate, we adopt the "standard" model of $R_V = 3.1$. This sets the reddening vector $\boldsymbol{R}_F = (4.11, 3.10, 1.85, 0.64)$ for B, V, I, and F160W, respectively. However, it is not necessary to fix R_V to a specific value because we have 4 band photometry, and we explore how changing this parameter affects our distance modulus by varying it on a grid from $R_V = 2.5$ to 6.5. For each value of R_V, we calculate the extinction vector $\boldsymbol{R}_F$ from the Cardelli et al. (1989) extinction law and refit the data, using the over-all minimum value of χ^2 as an estimate of the best fit.

4.1 Metallicity dependence

For studying the effects of metallicity on Cepheid mean magnitudes, we only need accurate differential metallicities – the absolute metallicities are unimportant. In the context of the present study, the relative mean metallicity of LMC Cepheids and our sample impacts the determined distance modulus, while the variation of metallicities within our sample determines the metallicity dependence of the Cepheid mean magnitudes. As given in Equation 8, the generic form of the metallicity effect is $\boldsymbol{\gamma}(Z_i - Z_{LMC})$ where Z_i is the estimated metallicity of the NGC 4258 Cepheid i and Z_{LMC} is the reference metallicity of the LMC. For the Cepheids in NGC 4258, we estimate their metallicity based on a linear fit to H II region abundances with radius, combined with the radial position of the Cepheid. The deprojected galactocentric radius $\rho = \left(x^2 + y^2\right)^{1/2}$ of a Cepheid is given by

$$\begin{pmatrix} x \\ y \end{pmatrix} = \begin{pmatrix} \cos\phi & \sin\phi \\ \frac{-\sin\phi}{\cos i} & \frac{\cos\phi}{\cos i} \end{pmatrix} \begin{pmatrix} \delta - \delta_0 \\ (\alpha - \alpha_0)\cos\delta \end{pmatrix} \quad (10)$$

where δ and α are the Declination and Right Ascension of a given Cepheid, and $\delta_0 = 47^\circ 18' 14\farcs30$ and $\alpha_0 = 12^h 18^m 57.50^s$ are the Declination and Right Ascension of the center of NGC 4258. We adopted a position angle $\phi = 150^\circ$, an inclination angle $i = 72^\circ$, and an isophotal radius $\rho_0 = 7\farcm92$ (van Albada 1980).

H II region metallicities for NGC 4258 are available from Z94 and Bresolin (2011a, hereafter B11), but there are several complications. The first is the paucity of H II regions and the resulting uncertainties in any estimate of the linear trend. In our quantitative results, we address this issue using the approach of G11. Given a set of H II regions, we fit a linear trend directly to the abundances and use that gradient for the fits in Equation 8. We include the uncertainties in the gradient by bootstrap resampling over the H II regions (as well as the Cepheids) and refitting the linear trend of the bootstrap-resampled data. This method naturally includes all the statistical uncertainties associated with the metallicity and its slope. We also allow the LMC metallicity to vary by a Gaussian deviate of 0.08 when we do the bootstrap resampling (see G11).

The second problem is the systematic question of which metallicity scale to use. Metallicity gradients can only be compared using samples with the same absolute calibrations. Most H II region metallicity estimates are based on "strong line" estimates, which have significant uncertainties in their absolute calibrations. In NGC 4258, there are only 4 H II regions with "direct" measurements using detections of the faint [OIII]λ4363 auroral line. The original Z94 (strong line) oxygen abundance gradient is

$$Z_i = 12 + \log(\mathrm{O/H}) = 9.17 - 0.49\rho_i/\rho_0, \quad (11)$$

while B11 found a significantly shallower gradient (after converting to our standard $\rho_0 = 7\farcm92$ isophotal radius) of

$$Z_i = 12 + \log(\mathrm{O/H}) = 8.87 - 0.20\rho_i/\rho_0 \quad (12)$$

for the strong line method (from the photoionization models of McGaugh 1991 and Kuzio de Naray et al. 2004) and

$$Z_i = 12 + \log(\mathrm{O/H}) = 8.49 - 0.18\rho_i/\rho_0 \quad (13)$$

based on strong lines calibrated to the few auroral line measurements (the empirical system of Pilyugin & Thuan 2005). If we transform all the B11 strong line measurements to the Z94 system, following Kewley & Ellison (2008), we find

$$Z_i = 12 + \log(\mathrm{O/H}) = 9.06 - 0.28\rho_i/\rho_0. \quad (14)$$

When we change between these calibration scales, we must also be sure that the reference metallicity for the LMC is on the same scale. The traditional value of $Z_{LMC} = 8.5$ is essentially a strong line estimate and should not be used with the auroral line calibrated metallicities. Essentially, the auroral line measurements provide well-constrained estimates of the electron temperatures, so a comparable measurement for the LMC is the estimate of $Z_{LMC} = 8.25$ from detailed models of the 30 Doradus region by Pellegrini et al. (2011).

Combining all these issues, we will consider three different metallicity models, combined with the bootstrap resampling methods given above. First, in the Z94-1 model, we simply combine the original Z94 data with $Z_{LMC} = 8.5$ (so as to better compare our results with M06). Second, in the Z94-2 model, we transform the B11 H II region data to the Z94 system and use the combined set of H II regions, again with $Z_{LMC} = 8.5$. Finally, in the B11-e model, we transform the Z94 H II region data to the auroral B11 system and use $Z_{LMC} = 8.25$. After bootstrap re-sampling the H II regions, we found gradients consistent with those presented in B11, with $Z_i = (9.06 \pm 0.03) - (0.30 \pm 0.05)\rho_i/\rho_o$ in the Z94-2 system and $Z_i = (8.51 \pm 0.02) - (0.19 \pm 0.04)\rho_i/\rho_o$ in the B11-e system.

5 RESULTS

We start with the "standard" model, in which we fit individual Cepheid extinctions. Then, in §5.1, we allow the extinction law to vary, and in §5.2 we examine the role of metallicity. Figure 4 displays the extinction-corrected mean magnitudes and the best-fit PL relations, adjusted to the appropriate distance modulus. We found $\Delta\mu_{LMC} = 10.72 \pm 0.04$ mag, after rescaling the uncertainties by a factor of 1.84 to make $\chi^2/dof = 1$. After correcting for extinction and examining the residuals of the Cepheid mean magnitudes from the fit, we found three Cepheids significantly offset from the F160W PL relation. Based on their measurement uncertainties, Cepheids 5, 32, and 38 are 3.8σ, 7.7σ, and 7.9σ outliers from the F160W PL relation, respectively, and all are over 1.5 mag fainter than the F160W PL relation. The outliers are displayed as open circles in Figure 4. If we clip these Cepheids from the sample and refit the data, we find $\Delta\mu_{LMC} = 10.70 \pm 0.03$ mag, and we only need to rescale the uncertainties by a factor of 1.38. Using this smaller rescaling factor, we fix the uncertainties on the remaining Cepheids and exclude Cepheids 5, 32 and 38 from the rest of

the study, bringing our final LBT sample to 40 Cepheids. Bootstrap resampling these 40 Cepheids yields $\Delta\mu_{LMC} = 10.71 \pm 0.06$ mag.

The best fit combines the OGLE II BVI PL relations (Udalski et al. 1999) with the Persson et al. (2004) F160W interpolated PL relation. Table 5 summarizes the effects of different combinations of PL relations on the distance modulus. We found that the distance modulus is relatively insensitive to the choice of PL relations. The only exception is using the Ngeow et al. (2009) I band PL relation, which drives $\Delta\mu_{LMC}$ down by ~ 0.10 magnitudes. As previously mentioned, there is moderate tension in the I band PL relation determinations from the OGLE II and Ngeow et al. (2009) studies, with the differences attributed to varying treatments of extinction. Using the OGLE II BVI PL relations improves χ^2/dof by $0.01 - 0.11$. Our fit has 98 degrees of freedom, which gives $\langle \sigma_{\chi^2/dof} \rangle = (2/dof)^{1/2} = 0.14$, so we cannot statistically distinguish between the PL relations. We also do not find a strong preference for the long-period PL relations from Sandage et al. (2004) and Ngeow et al. (2009), although we cannot rule out these PL relations, either. Comparing all of these cases, we adopt PL relations that produce the global minimum value of χ^2, corresponding to the OGLE II optical and Persson et al. (2004) interpolated F160W PL relations, which are are shown with the 1σ rms scatter of the data in Figure 4. Since the F160W band is the *HST* analog of the standard near IR H band, we refer to it as the "H" band for the remainder of this section, although the effective wavelength of this filter is slightly offset from that of the H band.

The LMC PL relations are nominally corrected to zero extinction, although there could be some residual contribution due to imperfect corrections. Only 2 NGC 4258 Cepheids had a reddening lower than the foreground Galactic reddening of $E(B-V) = 0.016$ mag, estimated from the Schlegel et al. (1998) dust map. Cepheid 9 had $E(B-V) = 0.01 \pm 0.01$ mag, and Cepheid 41 had $E(B-V) = -0.03 \pm 0.02$ mag. While a negative reddening is unphysical, these values could be explained by photometric errors rather than systematic effects (e.g., a blended blue star).

It is instructive to compare our fitting procedure to a simpler model which employs a single mean extinction applied to all Cepheids (as well as the common distance modulus). Figure 5 shows the residuals of this fit, which are highly correlated in the direction of the reddening vector, as expected for differential extinction. We can characterize the residuals using the covariance matrix

$$c_{ij} = \mathrm{covar}\left[(\hat{m}_i - \langle m \rangle_i^{PL})(\hat{m}_j - \langle m \rangle_j^{PL})\right] \tag{15}$$

and the vector

$$c_{ii}^{1/2} = \begin{pmatrix} B & V & I & H \\ \sigma_B & \sigma_V & \sigma_I & \sigma_H \end{pmatrix} \tag{16}$$

where i and j run over the filters B, V, I, and H, and σ_{ii} is the rms of the residuals in the appropriate filter (in magnitudes). For this model, with only a mean extinction (rather than individual extinction solutions), the formal covariances between filters are

$$\frac{c_{ij}}{(c_{ii}c_{jj})^{1/2}} = \begin{pmatrix} 1.00 & 0.88 & 0.74 & 0.32 \\ 0.88 & 1.00 & 0.87 & 0.37 \\ 0.74 & 0.87 & 1.00 & 0.63 \\ 0.32 & 0.37 & 0.63 & 1.00 \end{pmatrix}. \tag{17}$$

with

$$c_{ii}^{1/2} = \begin{pmatrix} B & V & I & H \\ 0.36 & 0.29 & 0.24 & 0.33 \end{pmatrix}. \tag{18}$$

Here, the vector shows the amplitudes of the residuals for each filter and the normalized matrix $c_{ij}/(c_{ii}c_{jj})^{1/2}$ shows the strength of the correlations, where values of 0, 1, and -1 mean no correlation, perfect correlation, and perfect anti-correlation, respectively. For comparison, Figure 6 displays the residuals of our fit using individual extinctions for each Cepheid. These residuals have no component parallel to the reddening vector because the fitting procedure will model out all variations in this direction. The formal covariance matrix now shows much weaker correlations with

$$\frac{c_{ij}}{(c_{ii}c_{jj})^{1/2}} = \begin{pmatrix} 1.00 & -0.20 & -0.54 & -0.23 \\ -0.20 & 1.00 & -0.23 & -0.31 \\ -0.54 & -0.23 & 1.00 & 0.57 \\ -0.23 & -0.31 & 0.57 & 1.00 \end{pmatrix} \tag{19}$$

and

$$c_{ii}^{1/2} = \begin{pmatrix} B & V & I & H \\ 0.12 & 0.03 & 0.11 & 0.29 \end{pmatrix}. \tag{20}$$

Note, however, that the extinction corrections have done little to reduce the variance of the H band residuals.

The remaining correlations represent the components of all systematic effects that cannot be modeled as extinction. There is no simple, intuitive means of interpreting these residuals since they may be due to multiple systematic effects, each with a component degenerate with extinction and distance. G11 approached this problem by projecting their residuals onto a vector $\boldsymbol{E}_2$ orthogonal to the reddening vector $\boldsymbol{R}_F$ and distance vector $\boldsymbol{\mu} = (1, 1, 1, 1)$. In this reduced error space, they found a color dependence of the PL relations, which was also correlated with galactocentric radius, and was therefore interpreted as a metallicity effect. However, with 4 band photometry, this method would require 2 orthogonal vectors, which has no intuitive physical interpretation. Instead, we perform a principle component analysis (PCA) on the residuals, and find eigenvalues of 0.092, 0.016, 0.005, and 0.001. This implies that there is a single, preferred direction of the residuals, which lies in the direction

$$\boldsymbol{p}_1 = \begin{pmatrix} B & V & I & H \\ -0.12 & -0.03 & 0.24 & 0.96 \end{pmatrix}. \tag{21}$$

The largest part of this component is a consequence of the H band residuals, which is problematic because of our incomplete photometric coverage. While the correlations between the H band and the other filters only make use of the 21 Cepheids for which we have 4-band data, the aggregate covariance matrix includes all 40 Cepheids in BVI. Thus, the structure of $\boldsymbol{p}_1$ is extremely sensitive to the residuals from the sub-sample of 21 Cepheids with 4 band photometry, and projections of the residuals onto $\boldsymbol{p}_1$ are not strictly defined for the 19 Cepheids without H band measurements. As an alternative to using incomplete 4-band photometry, we estimated $\boldsymbol{p}_1$ by refitting the BVI data alone and calculating the covariance matrix from nearly complete 3-band photometry (only 2 Cepheids are missing B band measurements). In this alternative fit, we find that $\mu = 10.72 \pm 0.03$ mag, in agreement with our previous estimate ($\chi^2/dof = 0.83$), and the covariance matrix becomes

$$\frac{c_{ij}}{(c_{ii}c_{jj})^{1/2}} = \begin{pmatrix} 1.00 & -0.20 & -0.53 \\ -0.20 & 1.00 & -0.21 \\ -0.53 & -0.21 & 1.00 \end{pmatrix} \tag{22}$$

and

$$c_{ii}^{1/2} = \begin{pmatrix} B & V & I \\ 0.12 & 0.03 & 0.11 \end{pmatrix}. \tag{23}$$

These covariances are in good agreement with those in equation 19, and the eigenvalues of this matrix are 0.021, 0.007, and 0.001, again

implying a single dominant direction of the residuals. However, the direction of this principal component is

$$\boldsymbol{p}_{BVI} = \begin{pmatrix} B & V & I \\ 0.75 & -0.01 & -0.66 \end{pmatrix} \quad (24)$$

substantially different from the hyperplane defined by the BVI components of $\boldsymbol{p}_1$. Despite this change, $\boldsymbol{p}_{BVI}$ does share some of the characteristics of $\boldsymbol{p}_1$, particularly a small V component and a noticeable anti-correlation between B and I.

The result of $\Delta\mu_{LMC}$ =10.70 ± 0.03 mag using the LBT Cepheids and individual extinctions is in excellent agreement with the distance determined by M06 from the inner field Cepheids of $10.71\pm0.04_{stat}\pm0.05_{sys}$ mag, but is in tension with the outer field distance of $10.87 \pm 0.05_{stat} \pm 0.05_{sys}$ mag. These distances were derived by averaging the reddening-free distance modulus of each Cepheid in the relevant field, and M06 attributed the difference between the fields to their different locations, and hence metallicities. The LBT Cepheids provide a means of testing the relation between inferred distance and galactocentric position, since they are drawn from a wide range of azimuthal angles and radial distances. The LBT Cepheids run from 0.22-1.54ρ_0, a much larger range of radii than the location of the outer field (centered at 1.02ρ_0). First, we searched for trends in the PL residuals as a function of galactocentric radius, and the results are shown in Figure 7, while Table 6 summarizes the results of performing a linear least squares fits to the residuals as a function of radius. There is a slight negative slope in the B band residuals, and a slight positive slope in the I band residuals. This suggests that the Cepheid spectral energy distributions (SEDs) are shifting towards the blue with increasing galactocentric radius. G11 found a similar result in M81, and they note that this could be due to less line-blanketing in metal-poor Cepheids near the galaxy's periphery. As with the G11 result, Kochanek (1997) found that metal-poor Cepheids tend to be bluer than metal-rich Cepheids, which matches theoretical expectations (Chiosi et al. 1993; Marconi et al. 2005). In order to check for any impact on the distance modulus, we tried binning the LBT Cepheids in radius, and fit all Cepheids with $0.22 \leq \rho_i < 0.60$, $0.60 \leq \rho_i < 1.00$, and $1.00 \leq \rho_i < 1.54$ separately. We found $\Delta\mu_{LMC}$ =10.72 ± 0.06 mag in the first bin (10 Cepheids), $\Delta\mu_{LMC}$ =10.62 ± 0.05 mag in the second bin (15 Cepheids), and $\Delta\mu_{LMC}$ =10.78 ± 0.04 mag in the third bin (15 Cepheids). The dependence of the distance modulus on galactocentric radius is therefore unclear at this stage, and we return to this issue in §5.2.

Next, we fit the combined sample of LBT and M06 Cepheids, using the LBT results for the Cepheids in common. We used the final sample of 89 Cepheids used by M06, giving us a total of 122 Cepheids (seven Cepheids were matched between samples). We first fit the M06 Cepheids separately, so as to estimate the intrinsic scatter of this data about the PL relations, and found a rescaling factor of 4.42 based on χ^2/dof for this fit. After rescaling the M06 uncertainties (the LBT Cepheids have already been rescaled based on the initial fit), we found $\Delta\mu_{LMC}$ =10.73 ± 0.01 mag, and χ^2/dof =1.00. Bootstrapping the full Cepheid sample yields $\Delta\mu_{LMC}$ =10.73 ± 0.02 mag. These values are in good agreement with those determined from the LBT Cepheids alone, and the covariance matrix of this fit has a slightly different structure,

$$\frac{c_{ij}}{(c_{ii}c_{jj})^{1/2}} = \begin{pmatrix} 1.00 & -0.02 & -0.66 & -0.25 \\ -0.02 & 1.00 & -0.38 & -0.23 \\ -0.66 & -0.38 & 1.00 & 0.75 \\ -0.25 & -0.23 & 0.75 & 1.00 \end{pmatrix} \quad (25)$$

and

$$c_{ii}^{1/2} = \begin{pmatrix} B & V & I & H \\ 0.11 & 0.04 & 0.09 & 0.30 \end{pmatrix}. \quad (26)$$

Figure 7 also shows the residuals of the M06 data from the PL relations as a function of galactocentric radius. Using the combined data set, we find trends in the B and I bands consistent with those found with the LBT Cepheids alone but at a higher level of significance. In addition, if we exclude H band data of the LBT Cepheids and recalculate the covariance matrix, we find

$$\frac{c_{ij}}{(c_{ii}c_{jj})^{1/2}} = \begin{pmatrix} 1.00 & -0.02 & -0.65 \\ -0.02 & 1.00 & -0.37 \\ -0.65 & -0.37 & 1.00 \end{pmatrix} \quad (27)$$

and

$$c_{ii}^{1/2} = \begin{pmatrix} B & V & I \\ 0.11 & 0.04 & 0.09 \end{pmatrix}. \quad (28)$$

The vector defining the principal component is $\boldsymbol{p}_{BVI} = (0.80, 0.04, -0.60)$, which is remarkably similar to the direction derived from the BVI measurements of the LBT Cepheids alone. We return to the interpretation $\boldsymbol{p}_1$ and $\boldsymbol{p}_{BVI}$ in §5.2.

We also experimented with fits to a broken PL relation, since the M06 sample contains 12 Cepheids with $P < 10$ days. Using the Sandage et al. (2004) broken PL relations, we find that $\Delta\mu_{LMC} = 10.71 \pm 0.01$ mag with $\chi^2/dof = 1.01$, while the the broken PL relations from Ngeow et al. (2009) yield $\Delta\mu_{LMC} = 10.62 \pm 0.01$ mag with $\chi^2/dof = 1.19$. These results are in good agreement with our previous fits (again accounting for the Ngeow et al. 2009 I band PL relation, see Table 5). Since there are only 12 Cepheids with $P < 10$ days in the final M06 sample, it is likely that the 110 longer-period Cepheids overwhelm the fit. To check this hypothesis, we excluded the 12 short-period Cepheids, and refit the longer period Cepheids using both the broken and linear PL relations. We found that the distance modulus does not change when using the broken PL relations with the longer-period Cepheids alone, and that it decreases by only 0.01 mag when using the linear PL relations. These consistencies indicate that short-period Cepheids and any break in the PL relations have a minimal impact on our procedure.

5.1 Model 2 – varying the extinction law

Next, we refit the LBT Cepheids alone while allowing the extinction law to vary, and Figure 8 displays the best fit value of R_V and $\Delta\mu_{LMC}$, along with contours of the χ^2 surface. We find that the best fit parameters are $R_V = 4.9^{+0.9}_{-0.7}$, with $\Delta\mu_{LMC}$ =10.60 ± 0.03 mag. This value of R_V improved the fit by $\Delta\chi^2 = 9.60$. Bootstrap resampling the Cepheids yields $R_V = 4.8 \pm 1.7$ and $\Delta\mu_{LMC}$=10.60 ± 0.07 mag. As we would expect from the modest reduction in χ^2, we do not see a significant decrease in the strength of correlations between residuals in different bands:

$$\frac{c_{ij}}{(c_{ii}c_{jj})^{1/2}} = \begin{pmatrix} 1.00 & -0.14 & -0.49 & -0.15 \\ -0.14 & 1.00 & -0.38 & -0.38 \\ -0.49 & -0.38 & 1.00 & 0.46 \\ -0.15 & -0.38 & 0.46 & 1.00 \end{pmatrix} \quad (29)$$

and

$$c_{ii}^{1/2} = \begin{pmatrix} B & V & I & H \\ 0.13 & 0.03 & 0.10 & 0.29 \end{pmatrix}. \quad (30)$$

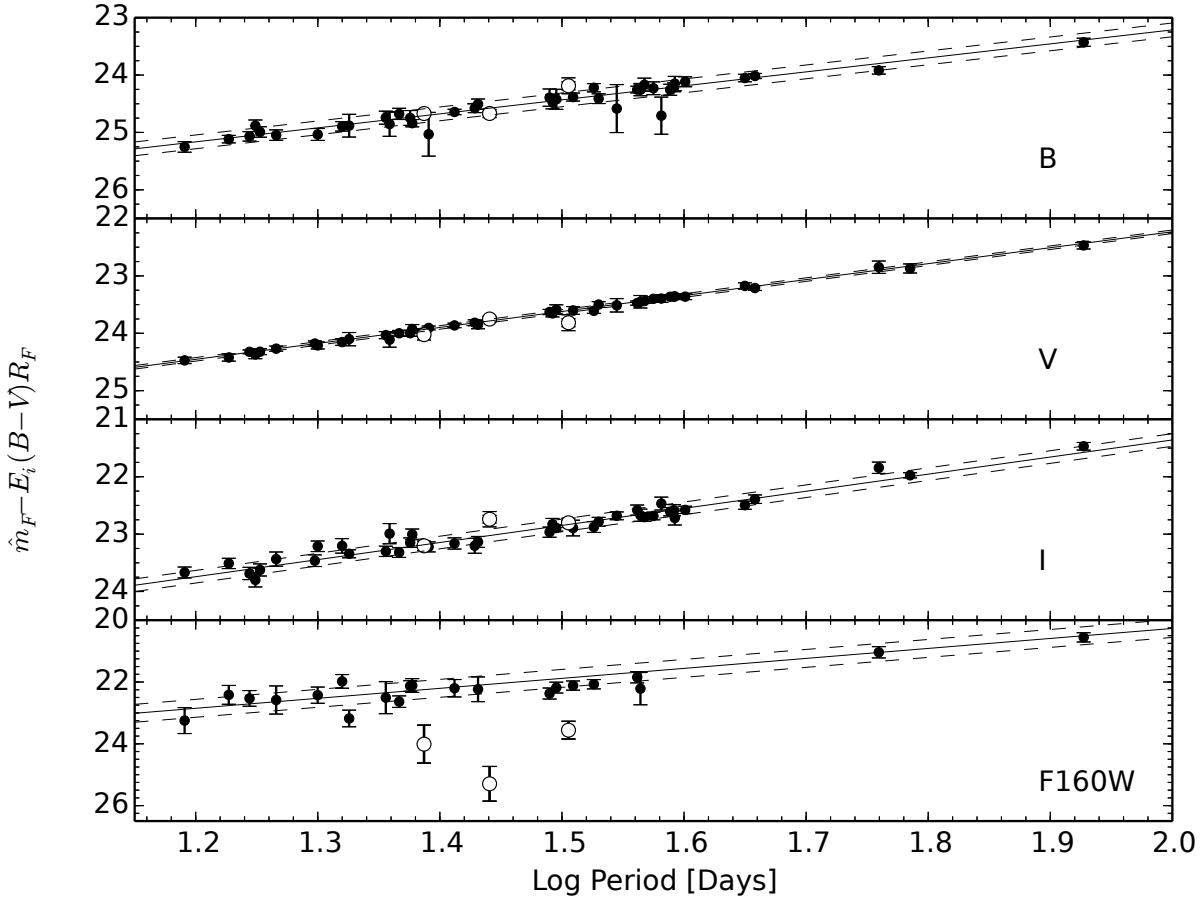

Figure 4. Four-band fit to PL relations from the LMC (solid lines), with extinction-corrected mean magnitudes, for Cepheids in NGC 4258. $\hat{m}_F$, $E_i(B-V)$, and R_F are defined in Equation 8. All variations in the direction of the extinction vector have been modeled out, leading to the reduced scatter (dashed lines, see text for details). The open circles mark the Cepheids that were removed due to large residuals from the F160W band PL relation, and are not included in the calculation of the scatter.

Varying R_V corresponds to fitting residuals in the direction

$$\frac{\partial \boldsymbol{R}_F}{\partial R_V} = \begin{pmatrix} B & V & I & H \\ -0.05 & 0.00 & 0.03 & 0.04 \end{pmatrix} \left(\frac{R_V}{3.1}\right)^{-2}, \quad (31)$$

and, as we see in Figure 6, this vector is not aligned with the residuals. Quantitatively, the dot product of the direction associated with $\boldsymbol{p}_1$ and the derivative of the extinction law with respect to R_V is only 8%, and so we would not expect changes in the extinction law to absorb very much of the principal component. If we include the M06 Cepheids, we find $\Delta\mu_{LMC} = 10.60 \pm 0.02$ mag with $R_V = 4.7^{+0.5}_{-0.4}$. For the Cardelli et al. (1989) extinction law and $R_V = 4.9^{+0.9}_{-0.7}$, the reddening vector is (5.91, 4.90, 3.26, 1.16) in B, V, I and F160W, respectively. If R_V were instead assumed to be 3.1, the extinctions in the I and F160W bands would be underestimated by 56% and 55%, respectively. While the magnitude of extinction in the near-IR is still several times smaller than in the optical, the grayer extinction law changes the distance modulus by 0.11 mag, which corresponds to a 5% change in the distance.

It would be dangerous to interpret our large value of $R_V = 4.9$ as an indication of the physical properties of the dust in NGC 4258. $R_V > 4.5$ is a condition realized for some sight-lines (both within the Milky Way and towards extra-galactic sources), but such extinction laws are usually associated with molecular clouds. For example, De Marchi et al. (2014) found $R_V \sim 5.6$ for a sight-line offset 6 arcminutes from 30 Dor in the LMC, and $R_V \sim 4.5$ within the nebula/HII region itself (although with a different functional form than the Cardelli et al. (1989) parameterization, see De Marchi & Panagia 2014). On the other hand, Gordon et al. (2003) found a mean value of $R_V = 3.41$ over the entire LMC, and Pejcha & Kochanek (2012) found a mean value of $R_V = 3.127$ for an aggregate sample of Galactic, LMC, and Small Magallenic Cloud Cepheids. Several of these studies also found some discrepancy between the Milky Way extinction law and those inferred for the LMC (De Marchi et al. 2014; De Marchi & Panagia 2014; Gordon et al. 2003), which highlights the systematic issues associated with assuming a universal extinction law.

With this discussion in mind, we find it unlikely that a physical reason explains why the mean extinction law across the entire disk of NGC 4258 would be parameterized by $R_V = 4.9$. The large value of R_V likely indicates that the Cepheid data prefer some kind of color correction. This could be due to a number of factors, for example, systematic photometric errors in a single pass-band,

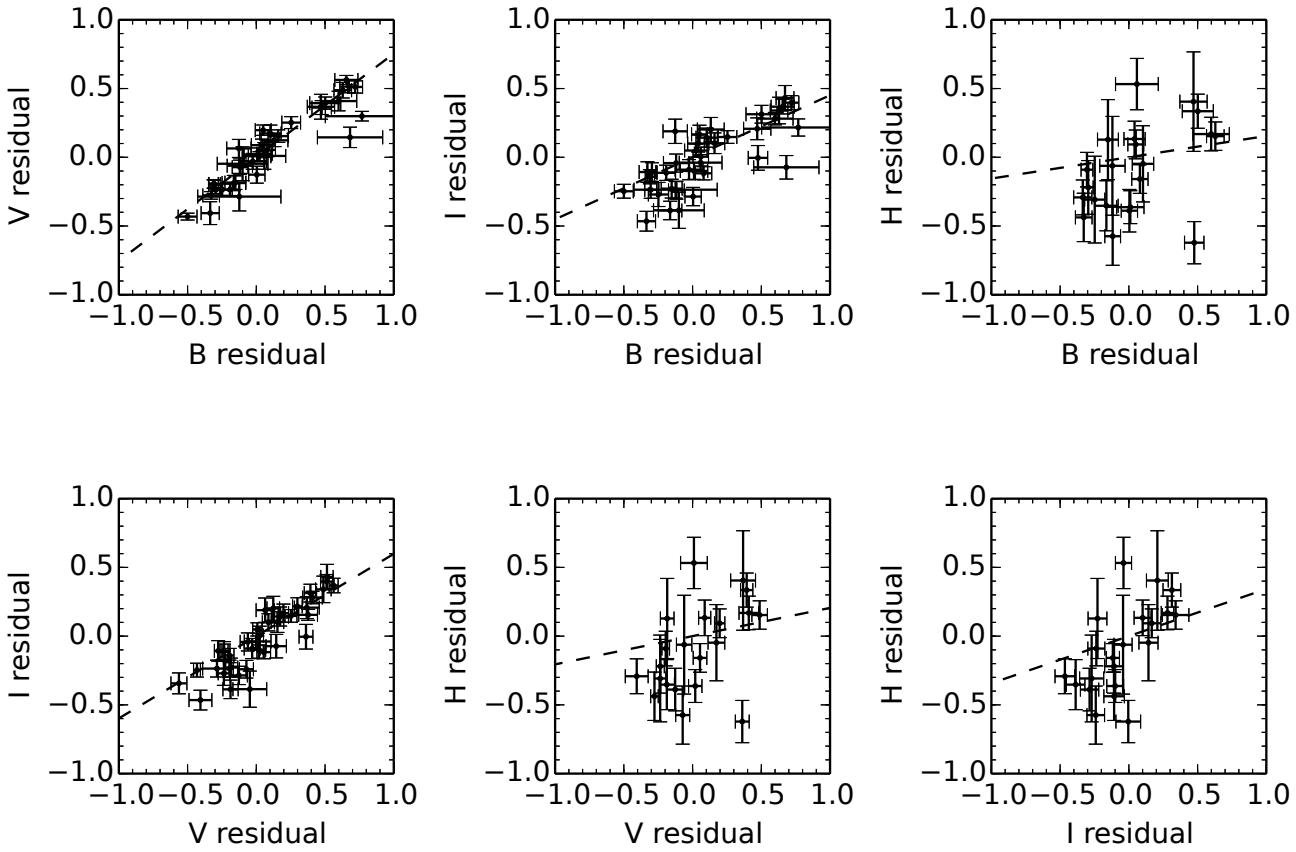

Figure 5. Projected residuals from the PL relations after fitting a mean extinction and the distance modulus. The residuals are dominated by the effects of differential extinction and thus are parallel to the correlations expected for a Cardelli et al. (1989) extinction law with $R_V = 3.1$, shown by the dashed lines.

or mistakes in the adopted PL relations. In fact, multiple systematic effects, including true variations in the extinction law, may be operating simultaneously. Given the extremely gray extinction law implied by $R_V = 4.9$, it seems probable that at least one other systematic effect is at work in our sample's colors. We pursue the question of peculiar Cepheid colors further in §5.2.

5.2 Model 3 – metallicity effects

In general, metallicity may affect both the mean magnitudes and the colors of the Cepheids. This means that we must allow the distance modulus as well as the mean magnitudes in each filter to vary based on the Cepheid metallicities, which can be accomplished by setting

$$\boldsymbol{\gamma} = (\gamma_1 \boldsymbol{\mu} + \gamma_2 \boldsymbol{c})(Z_i - Z_{LMC}) \quad (32)$$

where $\boldsymbol{\mu} = (1, 1, 1, 1)$ corresponds to metallicity effects that change the distance but not the color, and $\boldsymbol{c}$ is a vector quantifying the magnitude of the metallicity effect in each pass band. Most Cepheid studies have only examined the effects of γ_1 and simply assume that $\gamma_2 \equiv 0$. So as to compare our results with these studies, we first set $\gamma_2 \equiv 0$ and solve for γ_1. In subsequent models, we solve for both parameters. However, $\boldsymbol{c}$ is not known *a priori*, and some component of this vector is probably degenerate with extinction. We know that our residuals are dominated by a single principal component, either $\boldsymbol{p}_1$ or $\boldsymbol{p}_{BVI}$, and we will therefore experiment with models where $\boldsymbol{c} = \boldsymbol{p}_1$ or $\boldsymbol{p}_{BVI}$.

For the LBT Cepheids alone, Table 7 shows the results of incorporating γ_1 with $\gamma_2 \equiv 0$ and testing models with R_V equal to both 3.1 and 4.9. For simplicity, we only discuss the results for $R_V = 3.1$, although the results for $R_V = 4.9$ can be found in Table 7. The inferred values of $\Delta\mu_{LMC}$ are 10.75 ± 0.05 mag, 10.80 ± 0.11 mag, and 10.74 ± 0.05 mag in the Z94-1, Z94-2, and B11-e models, respectively. The changing distance modulus is a consequence of systematic uncertainties associated with absolute metallicity measurements. The Z94-2 gradient ($\Delta\mu_{LMC} = 10.80 \pm 0.11$ mag) is shallower than that of Z94-1, which places NGC 4258 at a higher mean metallicity, and our model forces the distance modulus to absorb this offset. The shallower gradient also drives correlations between γ_1 and $\Delta\mu_{LMC}$, which results in a flatter slope around the minimum value of χ^2 and a larger uncertainty on $\Delta\mu_{LMC}$. However, in the B11-e model, the difference between the metallicity zeropoints is smaller than in Z94-2, which balances the effects of the shallower gradient.

We emphasize that these issues are a consequence of the assumed metallicity scale, while the effect of the relative Cepheid

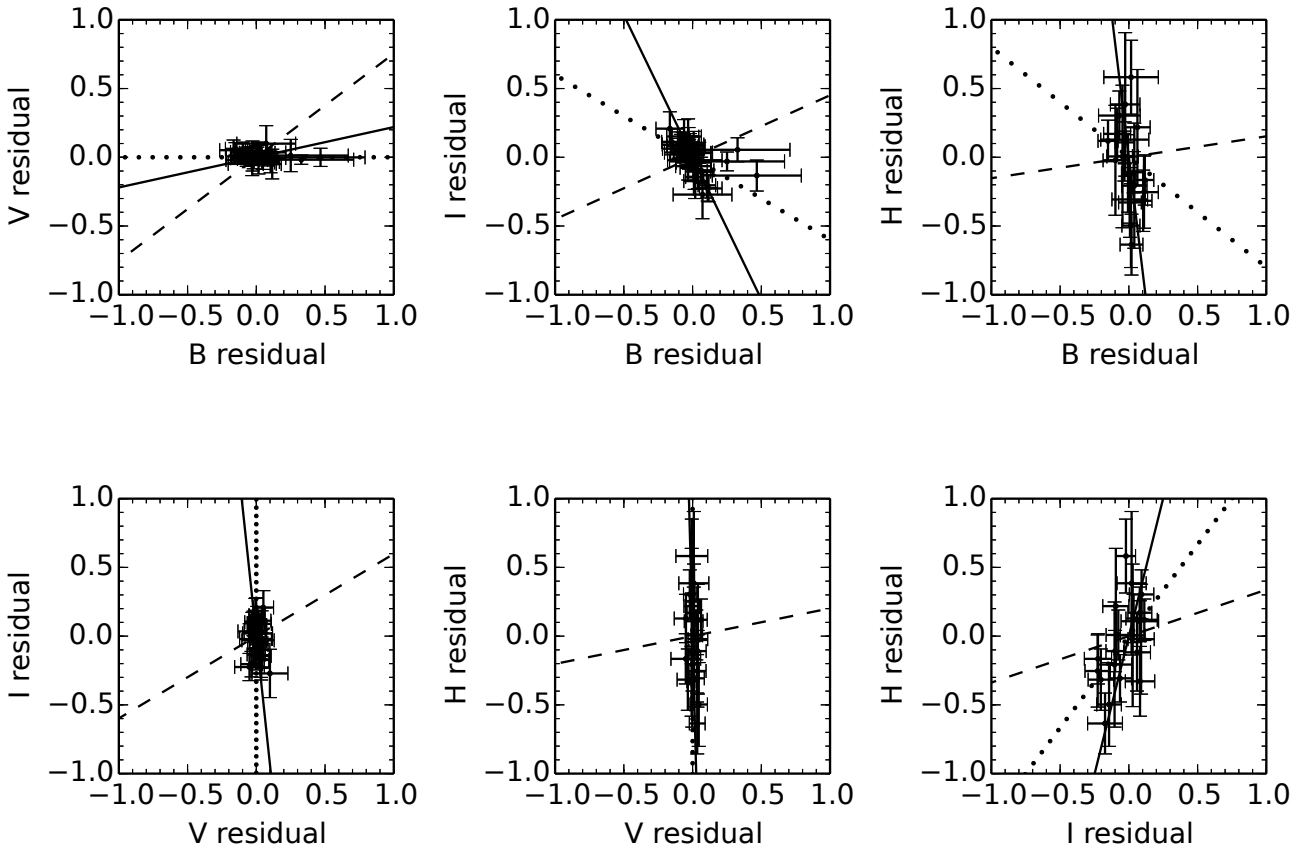

Figure 6. Projected residuals from the PL relations after fitting the individual extinctions and the mean distance. The solid lines show the direction of the dominant component from our principle component analysis. The dashed lines show the directions of the correlations due to differential extinction for $R_V = 3.1$. By definition, all correlations in this direction have been removed by fitting the individual extinctions. The dotted lines show the slope of the residuals expected for a change in the extinction law, $\partial \boldsymbol{R}_F / \partial R_V$. Since the Cardelli et al. (1989) extinction law in normalized to the V band, the V component is zero by definition.

metallicities is quantified by γ_1. We find that $\gamma_1 = -0.18 \pm 0.20$ mag/dex, -0.32 ± 0.35 mag/dex, and -0.50 ± 0.54 mag/dex in the Z94-1, Z94-2, and B11-e models, respectively. A shallower metallicity gradient implies a larger value of γ_1, as seen in the Z94-2 and B11-e models, since larger values of γ_1 can be used to compensate for a smaller range of Cepheid metallicities. The parameter uncertainties based on rescaled $\Delta\chi^2$ statistics continue to agree well with the bootstrap models, as can be seen in Table 7. Figure 9 shows the distribution of $\Delta\mu_{LMC}$ and γ_1 obtained from our bootstrap estimates. However, adding this metallicity term does not significantly reduce or change the covariance matrix of the residuals, since γ_1 is a correction applied in the direction $(1, 1, 1, 1)$, which cannot absorb any significant part of $\boldsymbol{p}_1$ or $\boldsymbol{p}_{BVI}$.

The sign of γ_1 is defined so that metal-rich Cepheids are intrinsically more luminous than their metal-poor counterparts (Equation 8), as is typically found in other Cepheid studies (e.g. M06 and Shappee & Stanek 2011). In order to compare our results with those of M06, we fit the LBT Cepheids alone, using the same metallicity gradient and extinction law. We find a smaller metallicity dependence of -0.18 ± 0.20 mag/dex, compared to their reported value of $-0.29 \pm 0.09_{stat} \pm 0.05_{sys}$ mag/dex. If we instead fit the combined LBT+M06 Cepheid sample, we find that $\gamma_1 = -0.24 \pm 0.08$ mag/dex with $\Delta\mu_{LMC} = 10.81 \pm 0.03$ mag, and $\chi^2/dof = 0.97$, in good agreement with the original findings of M06. We find $\Delta\mu_{LMC} = 10.89 \pm 0.06$ mag and $\gamma_1 = -0.42 \pm 0.14$ mag/dex for the Z94-2 model ($\Delta\mu = 10.98 \pm 0.10$ mag, $\gamma_1 = -0.61 \pm 0.21$ mag/dex with bootstrap resampling), and in the B11-e model, we find $\Delta\mu_{LMC} = 10.81 \pm 0.03$ mag and $\gamma_1 = -0.65 \pm 0.22$ mag/dex ($\Delta\mu_{LMC} = 10.88 \pm 0.09$ mag, $\gamma_1 = -0.95 \pm 0.35$ mag/dex with bootstrap resampling). The differences in the results between the rescaled χ^2/dof method and bootstrap resampling method may be due to outliers in the M06 data set. If we employ a 5-σ iterative clipping routine, we reject 19 M06 Cepheids, and find for the combined data set that $\Delta\mu_{LMC} = 10.89 \pm 0.06$ mag and $\gamma_1 = -0.42 \pm 0.14$ mag/dex in the Z94-2 model, with bootstrap resampling yielding $\Delta\mu_{LMC} = 10.90 \pm 0.08$ mag and $\gamma_1 = -0.49 \pm 0.17$ mag/dex. In the B11-e model, we find $\Delta\mu_{LMC} = 10.81 \pm 0.03$ mag and $\gamma_1 = -0.65 \pm 0.22$ mag/dex with the trimmed sample, while bootstrapping yields $\Delta\mu_{LMC} = 10.81 \pm 0.08$ mag and $\gamma_1 = -0.77 \pm 0.29$

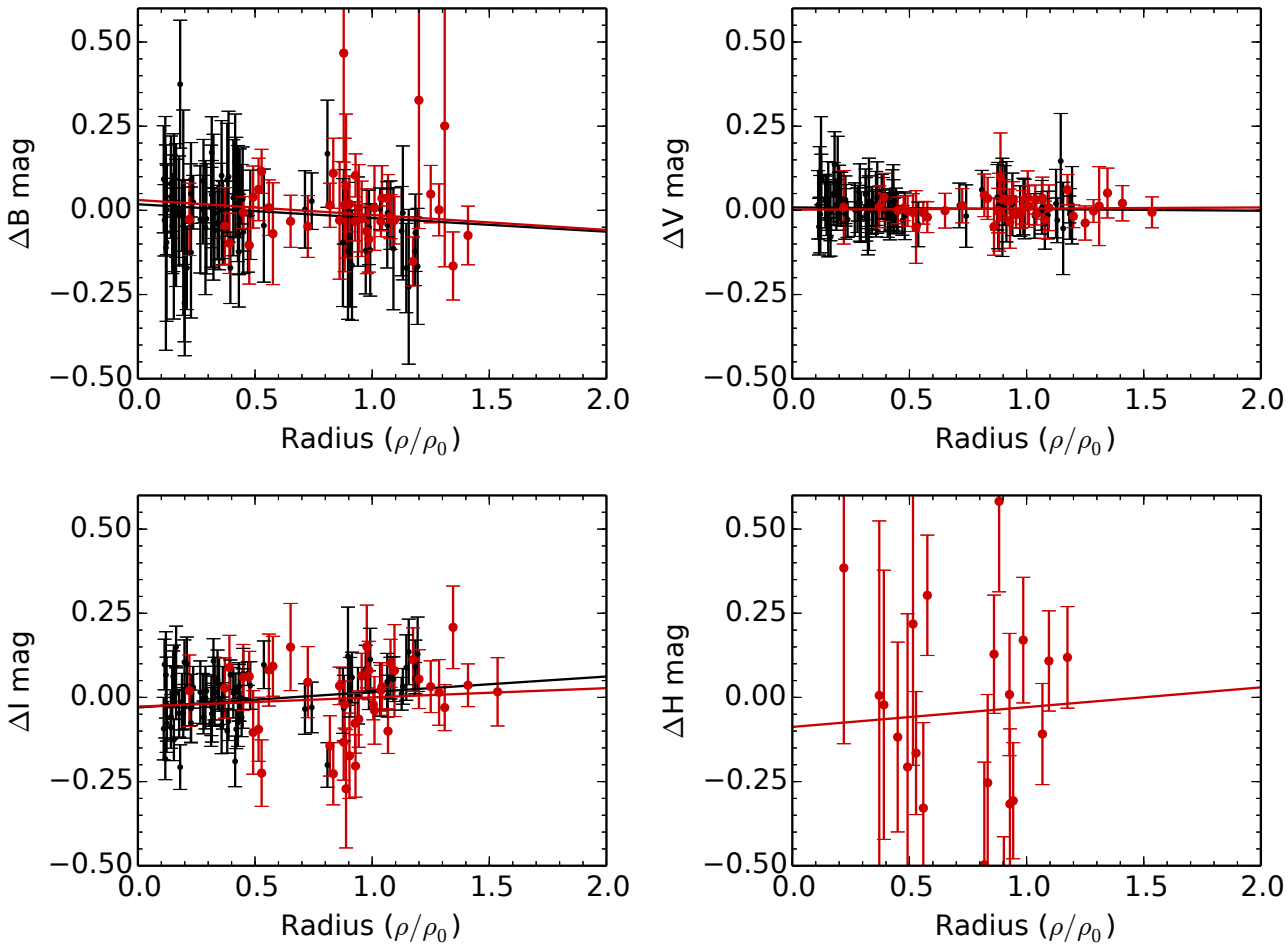

Figure 7. Residuals from PL relations as a function of galactocentric radius, in units of the isophotal radius, ρ_0. The LBT Cepheids are in red, the M06 Cepheids are the smaller black points. The red solid line is the result of a linear least-squares fit to the LBT Cepheids ($N = 40$), the black line is a fit to all Cepheids ($N = 122$). Note the stronger trends in the B and I bands when using the full sample. See Table 6 for results of the linear regression.

mag/dex. These values and their uncertainties are in much better agreement, although using the full set of 122 Cepheids still yields consistent results. We therefore retain the full set of M06 Cepheids for all of our models.

Figure 9 shows the bootstrap resampling distributions of $\Delta\mu_{LMC}$ and γ_1 for the combined sample. Generally speaking, the combined fit pulls the distance modulus ~ 0.15 mag higher and shrinks the uncertainties on γ_1 such that $\gamma_1 = 0$ is statistically ruled out. As can be seen in Figure 7, this is due to trends in the residuals from the PL relations with galactocentric radius that become more robust with the full sample.

Table 8 shows the results of fitting for γ_2 with $\boldsymbol{c} = \boldsymbol{p}_1$, and Figure 10 shows the bootstrapping distributions of γ_1 and γ_2. The LBT Cepheids alone do little to constrain either γ_1 or γ_2. However, we find that the combined LBT+M06 fit rules out $\gamma_1 = \gamma_2 = 0$ at $\gtrsim 99\%$ confidence, due to the shape of the error ellipse. In the Z94-1, Z94-2, and B11-e models, respectively, we find that $\gamma_1 = -0.00 \pm 0.15$ mag/dex, -0.20 ± 0.18 mag/dex, and 0.02 ± 0.43 mag/dex, while $\gamma_2 = -0.44 \pm 0.24$ mag/dex, -0.44 ± 0.22 mag/dex, and -1.23 ± 0.68 mag/dex. This is a 1.8-2σ detection of Cepheid color shifts with metallicity, and incorporating γ_2 obviates the need for a direct correction of the distance modulus. Because of the way in which $\boldsymbol{p}_1$ is defined, this correction implies that an increasing Cepheid metallicity results in a fainter BV magnitude and brighter I/F160W magnitude. However, we also note that the magnitude of the correction increases towards the near IR, contrary to theoretical predictions. In addition, the correction to the F160W band mean magnitudes is four times larger than in any other band, which is a result of our poor photometric coverage at this wavelength and the problematic definition of $\boldsymbol{p}_1$. Interestingly, changing the extinction law to $R_V = 4.9$ (and thereby changing the Cepheid colors) makes γ_2 consistent with 0, while γ_1 becomes significant at the 2.3-3.1σ level. This implies that Cepheid mean magnitudes must depend on metallicity, even if this effect is degenerate with a systematic color correction required by the data.

Figure 10 also shows the results of imposing a prior on $\Delta\mu_{LMC}$, based on the maser distance to NGC 4258 (Humphreys et al. 2013, $\mu_{N4258} = 29.40 \pm 0.06$ mag) and the eclipsing binary distance to the LMC (Pietrzyński et al. 2013, $\mu_{LMC} = 18.49 \pm 0.05$ mag). Our prior takes the form of a Gaussian probability distribution with mean 10.91 mag and width 0.08 mag, derived from adding the uncertainties of the independent distance estimates in quadrature. The results from the previous models are only discrepant with this value by about 2σ, and so the prior does little to

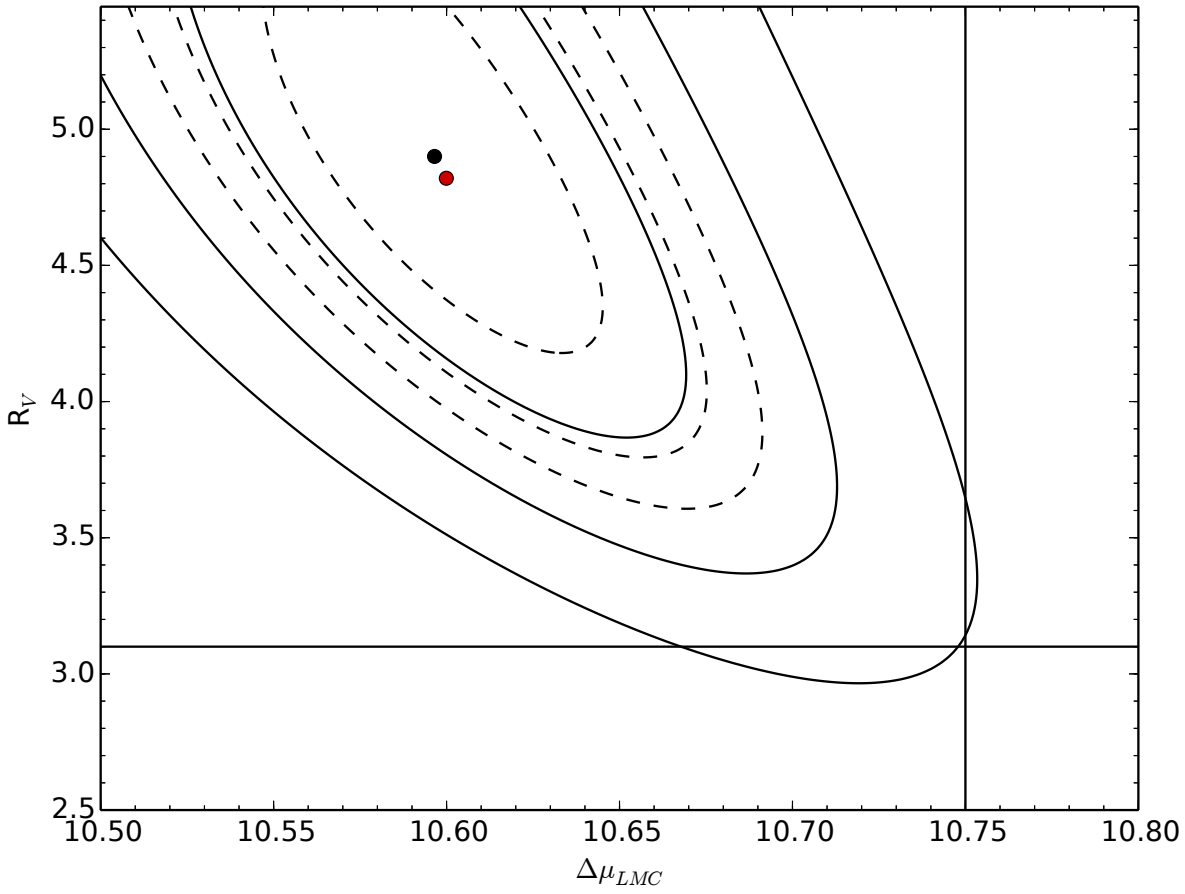

Figure 8. Contours of $\Delta\chi^2$ as a function of $\Delta\mu_{LMC}$ and R_V, using the LBT Cepheids only (N=40). The solid curves are the two-parameter 1, 2, and 3σ confidence intervals. The dashed curves are the same but for one parameter. The solid lines mark the standard value of $R_V = 3.1$ and the corresponding distance modulus. The red point is the median of the bootstrap resampling distribution.

constrain the data. The best fit parameters, estimated from bootstrap resampling, can be found in Table 10. We find that there is a slight effect on the LBT Cepheid sample, which increases the distance modulus by ~ 0.05 mag and slightly narrows the error ellipse for γ_1 and γ_2. The prior also shifts the values of γ_1 and γ_2 in a way that is consistent with the values inferred from the combined LBT+M06 sample, although the model still does not result in a significant detection of either parameter. The prior has no effect on the results of the combined sample, since they are already consistent with the value of 10.91 ± 0.08 mag.

After inspecting the covariance matrix for this fit, we found that this model does little to reduce the covariances between different bands. Essentially, this is because the residuals from model 1, projected onto the principle component $\boldsymbol{p}_1$, do not correlate very strongly with galactocentric radius, as shown in Figure 11. As noted in §5, $\boldsymbol{p}_1$ is only defined for 21 Cepheids, and most of the information in the data come from the BVI filters. In Figure 11 we also show the residuals projected onto $\boldsymbol{p}_{BVI}$ as a function of galactocentric radius for both the LBT and M06 Cepheids. After performing a linear least-squares fit, we again see a more significant slope, changing from -0.05 ± 0.05 using the LBT Cepheids alone to -0.05 ± 0.03 mag/ρ when using all 122 Cepheids, consistent with the trends in Figure 7.

Table 9 shows fits for γ_1 and γ_2 with $\boldsymbol{c} = \boldsymbol{p}_{BVI}$, and Figure 12 shows the bootstrap resampling distribution. At this stage, we only discuss the combined LBT+M06 sample, and we find that $\gamma_1 = -0.61 \pm 0.33$ mag/dex, -0.84 ± 0.35 mag/dex, and -1.69 ± 0.91 mag/dex, with $\gamma_2 = -0.20 \pm 0.18$ mag/dex, -0.22 ± 0.19 mag/dex, and -1.23 ± 0.68 mag/dex, in the Z94-1, Z94-2, and B11-e models, respectively ($\Delta\mu_{LMC} = 10.83 \pm 0.04$ mag, 10.91 ± 0.06 mag, and 10.83 ± 0.03 mag for these fits). While fits with 3-band photometry call for some adjustment to the distance modulus with metallicity, they are unable to tightly constrain any color effects.

In Figure 12 we also show the results of imposing a prior on $\Delta\mu_{LMC}$, and we find shifts in γ_1 and γ_2 using the LBT data alone that move these parameters closer to the the values obtained by fitting the larger sample. Furthermore, the LBT Cepheid sample in the Z94-2 metallicity model produces a metallicity effect of $\gamma_1 = -0.96 \pm 0.50$, detected at the 1.9σ level ($\gamma_2 = -0.30 \pm 0.18$), but all other results are still consistent with $\gamma_1 = \gamma_2 = 0$. The prior again has no effect on the combined Cepheid sample, since the results from these models are already consistent within the uncertainties.

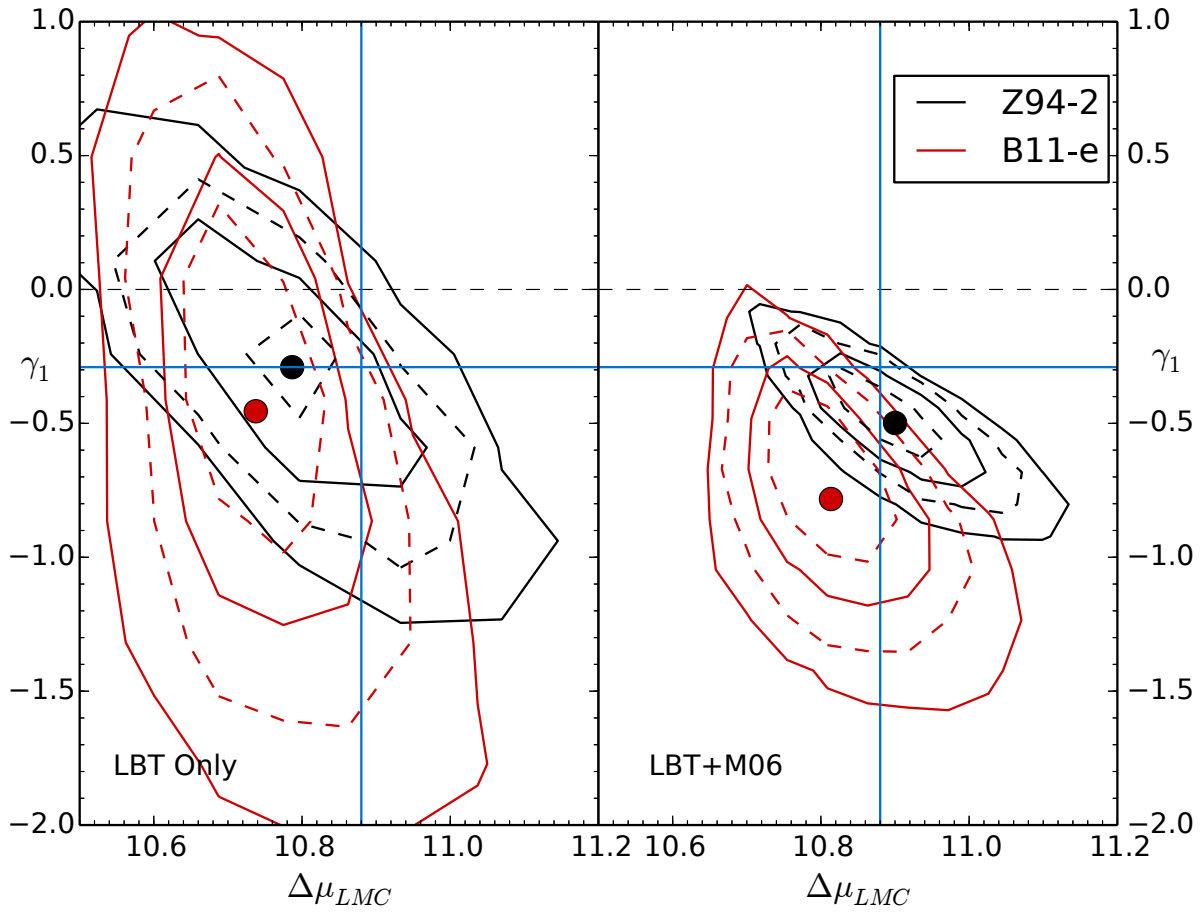

Figure 9. Distributions of $\Delta\mu$ and γ_1 obtained from bootstrap resampling. The left panel uses only the LBT Cepheids, while the right panel shows the combined LBT+M06 sample (N=122). The black lines are for the Z94-2 metallicity system, while the red contours are for the B11-e system. The solid contours are the 68% and 95% limits for two parameters, while the dashed contours mark the limits for a single parameter. The large circles mark the medians of the distributions, and the blue lines show the measurement from M06.

6 DISCUSSION AND CONCLUSIONS

6.1 Metallicity dependence of the PL relations

Our sample of 40 LBT Cepheids does not provide substantial evidence for a metallicity-dependent adjustment to the distance modulus of NGC 4258. The basic cause is the lack of any strong correlations of the residuals from the PL relations with galactocentric radius, used as a proxy for metallicity. This is exacerbated by the high inclination of NGC 4258's disk ($\sim 72^{\circ}$) and the shallow metallicity gradient (Bono et al. 2008, Bresolin 2011). However, if we combine our sample with the Cepheids found by M06, we find a statistically significant metallicity dependence of the mean magnitudes, at a value consistent with their estimate.

While the detection of the metallicity dependence using the combined data set is a robust feature of all the adopted metallicity scales, systematic uncertainties in the metallicity scales themselves limit the physical interpretation of this effect. We find mean magnitude corrections ranging from $\gamma_1 = -0.24 \pm 0.08$ mag/dex to -1.4 ± 0.45 mag/dex, depending on the metallicity system used to estimate the Cepheid compositions. Regardless of assumptions about how well the oxygen abundance gradient tracks the physical metallicity of the Cepheids, the broad range of parameter estimates for γ_1 illustrates how strongly metallicity measurement uncertainties affect estimates of the metallicity dependence of the PL relations, and perhaps accounts for the wide range of values found in the literature. Because the metallicity system used by Z94 is very prevalent, we report a final metallicity effect of $\gamma_1 = -0.61 \pm 0.21$ mag/dex, inferred from our bootstrap resampling of the H II regions and Cepheids in NGC 4258 using the Z94-2 model. This value takes appropriate measure of the uncertainties in both the metallicity gradient of NGC 4258 and the Cepheid mean magnitudes, is readily comparable with other studies, and is easily translatable into other metallicity systems. However, we note that there may be reasons to believe that other metallicity scales (e.g., the empirical electron temperature scale of B11) may be a more physical estimate of this effect.

There is a strong indication that both the LBT sample and the combined LBT+M06 sample prefer some adjustment to the Cepheid colors. This is evidenced by a decrease in χ^2 when using a grayer extinction law ($R_V = 4.9$), as well as the appearance of a single principle component in the residuals of our initial fitting procedure (fits for individual extinctions only). However, we

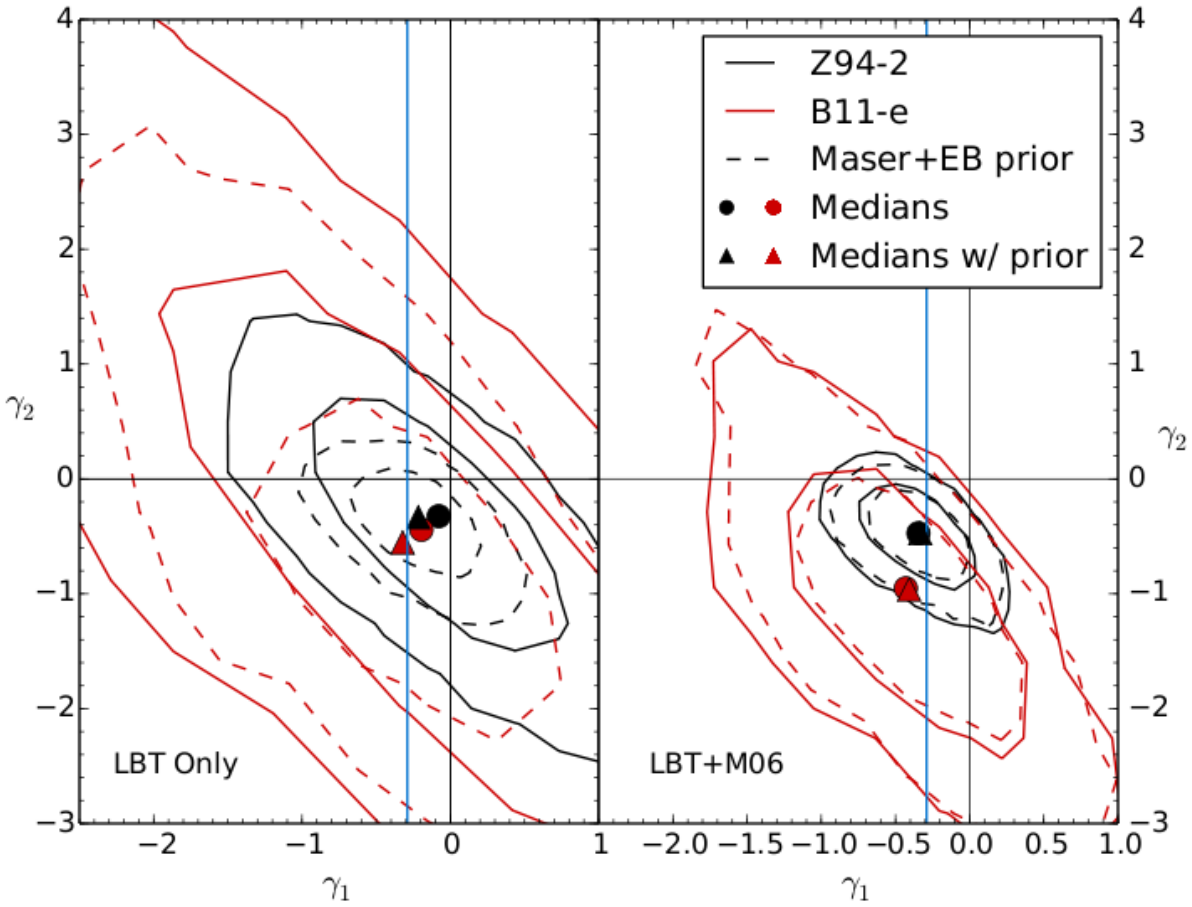

Figure 10. Distributions of γ_1 and γ_2 obtained from bootstrap resampling. The left panel uses only the LBT Cepheids and the right panel shows the combined LBT+M06 sample (N=122). The black lines are for the Z94-2 metallicity system, while the red contours are for the B11-e system. The vertical blue lines mark the value of γ_1 found by M06. The solid contours are the 68% and 95% limits for two parameters, while the dashed contours are the limits obtained by imposing a prior on $\Delta\mu_{LMC}$, based on the Pietrzyński et al. (2013) eclipsing binary distance for the LMC and the maser distance of NGC 4258 from Humphreys et al. (2013).

are unable to measure this component so as to uniquely determine its cause. Because of correlations between galactocentric radius and residuals from the B and I band PL relations (see Figure 7), part of this effect can be attributed to the varying metallicity of the Cepheids. However, our limited near-IR photometric coverage means that there is considerable uncertainty as to the magnitude of this effect in the F160W band, and we do not detect the metallicity-color correction using 3 band BVI photometry alone. On the other hand, a grayer extinction law removes the need for metallicity-dependent color corrections (although corrections to the distance modulus are still found), but the very large value of $R_V = 4.9$ suggests that this adjustment may be due to some other systematic effect beyond variations in the extinction law. For example, the adopted PL relations directly determine the expected Cepheid colors, so any errors in their determination (for example, due to interpolation or de-extinction procedures) could mimic variations in the extinction law. In order to disentangle these systematic effects, it appears that a larger sample with complete 4 band photometry is needed.

While this study has been predominately concerned with the effects of the extinction law and metallicity on Cepheid colors, other systematic effects exist that are expected to contribute to the problem. These include the difficulties of obtaining precise photometry of Cepheids in crowded fields, and, more importantly, the unknown systematic effects of blending due to stars physically associated with the Cepheids. To combat these issues, future studies will require a more thorough characterization of the Cepheid SEDs, with high quality data in many pass bands.

6.2 Calibration of the Cepheid PL relations

Calibrating the Cepheid PL relation is equivalent to determining an absolute distance to the LMC. This can be accomplished by means of the Humphreys et al. (2013) geometric maser distance to NGC 4258. Taking $\mu_{N4258} = 29.40 \pm 0.06$ mag (7.6 ± 0.23 Mpc), we calculate μ_{LMC} for each fit in Tables 7, 8, and 9. Figure 13 shows an alternative means of visualizing the data, by displaying the probability density functions (PDFs) for all estimates of $\Delta\mu_{LMC}$. The PDFs are taken to be univariate Gaussians, except for the bootstrapping estimates for which we show the (nor-

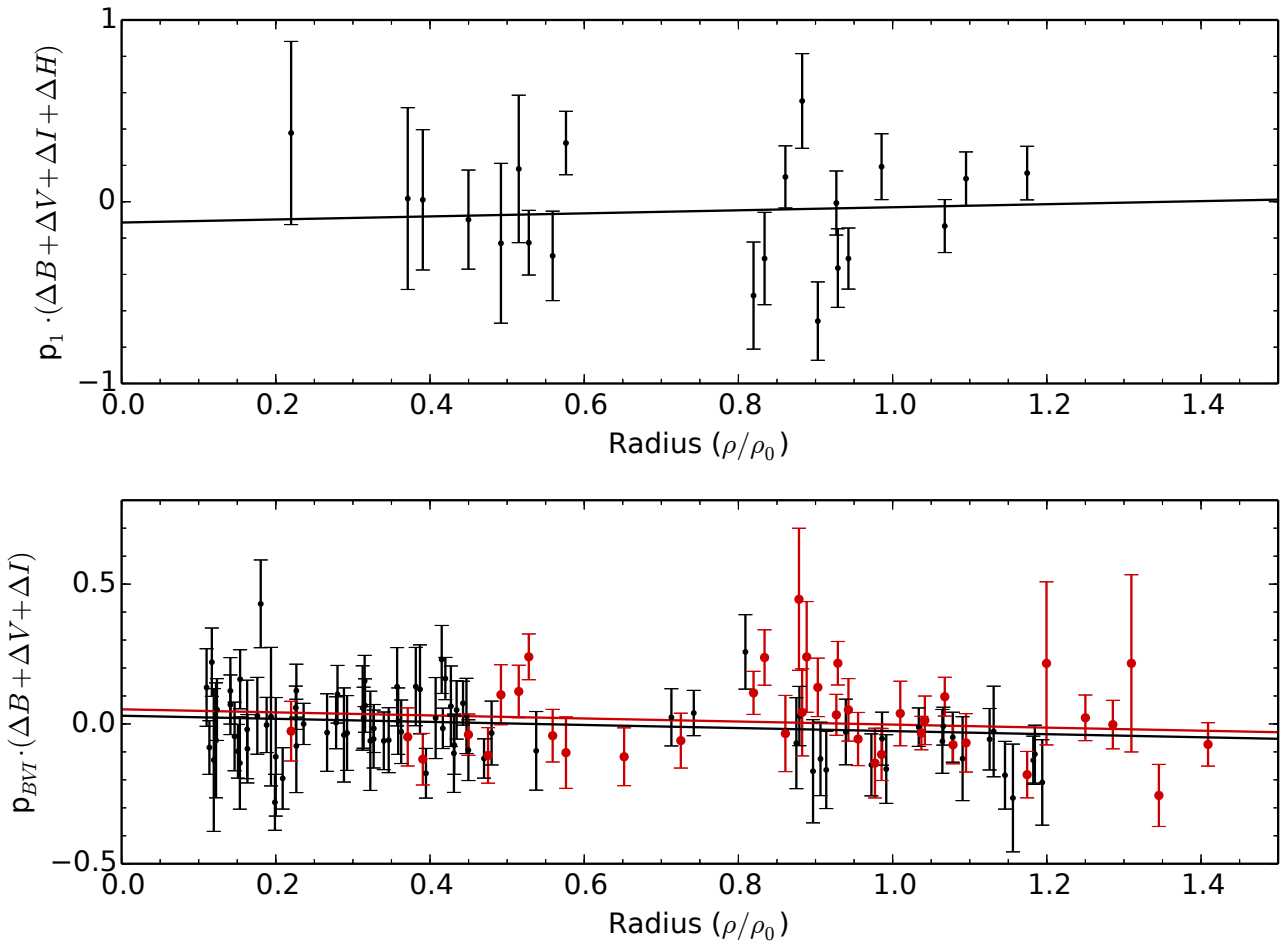

Figure 11. Residuals from the PL relations projected onto their principal components, as a function of galactocentric radius. The top panel includes all four filters, for which we only have 21 Cepheids. The bottom panel uses BVI only, and includes the LBT Cepheids in red and the M06 Cepheids as the small black points. The solid lines are the results of linear least-squares fits.

malized) posterior distributions. The vertical black line and shaded gray region mark $\Delta\mu_{LMC} = 10.91 \pm 0.08$ mag, determined from $\mu_{N4258} = 29.40 \pm 0.06$ (Humphreys et al. 2013) and $\mu_{LMC} = 18.49 \pm 0.05$ (Pietrzyński et al. 2013), with the uncertainties added in quadrature.

Although there are small differences in χ^2 for each fit, we have no strong evidence in favor of any of the particular models that we tried. However, we also note that including a metallicity effect tends to shift the Cepheid distance towards the value inferred by independent determinations, in some cases to within 0.01–0.02 mag (0.2–0.3σ). A conservative way to combine all of the results is to simply combine all the models with equal weight. Thus, if $P_i(\Delta\mu_{LMC})$ is the probability distribution for model i, we define the joint PDF as $(\sum P_i)/N$. This gives a particularly simple form for the mean and variance of the joint probability distribution

$$\langle\Delta\bar{\mu}_{LMC}\rangle = \sum_i^N \frac{\langle\Delta\mu_{LMC}\rangle_i}{N} \tag{33}$$

and

$$\langle(\Delta\bar{\mu}_{LMC} - \langle\Delta\bar{\mu}_{LMC}\rangle)^2\rangle = \tag{34}$$

$$\sum_i^N \frac{(\langle\Delta\mu_{LMC}\rangle_i - \langle\Delta\bar{\mu}_{LMC}\rangle)^2 + \sigma_i^2}{N} \tag{35}$$

where $\langle\Delta\bar{\mu}_{LMC}\rangle$ is the average of the means of the individual PDFs, and its variance is the quadrature sum of the rms scatter and the arithmetic mean of the intrinsic widths. We can interpret

$$\sigma_{stat} = \sqrt{\sum_i^N \frac{\sigma_i^2}{N}} \tag{36}$$

as an estimate of our statistical error, and

$$\sigma_{sys} = \sqrt{\frac{1}{N}\sum_i^N (\langle\Delta\mu_{LMC}\rangle_i - \langle\Delta\bar{\mu}_{LMC}\rangle)^2} \tag{37}$$

as an estimate of our systematic uncertainties.

We include all PDFs shown in Figure 13, but separate the PDFs derived from the LBT Cepheids only and the combined LBT+M06 sample. If we use only the LBT Cepheid PDFs, we find $\langle\Delta\bar{\mu}_{LMC}\rangle = 10.70 \pm 0.08_{stat} \pm 0.06_{sys}$, while for the combined

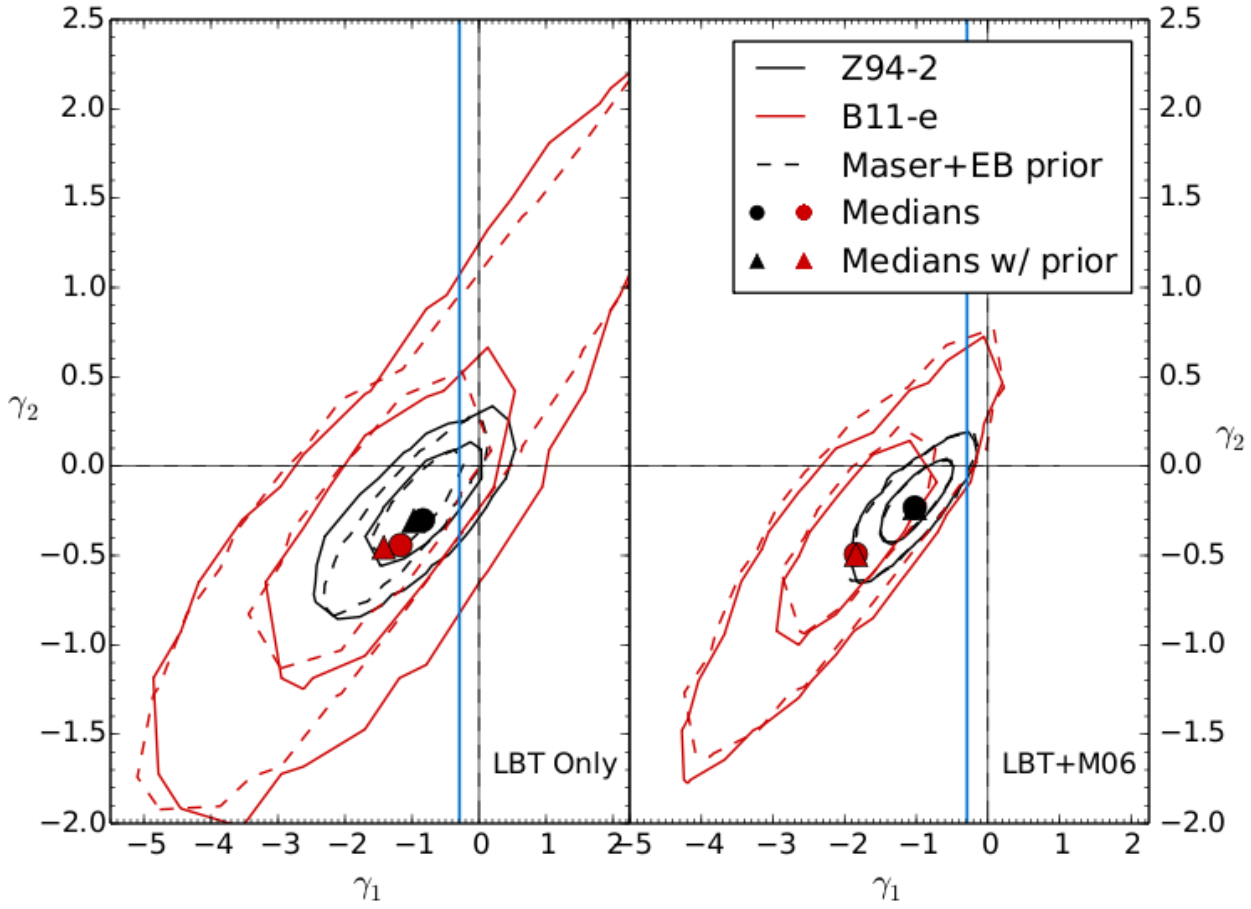

Figure 12. Distribution of γ_1 and γ_2 obtained from bootstrap resampling and setting $\boldsymbol{c} = \boldsymbol{p}_{BVI}$, using only the BVI data. The left panel uses the 40 LBT Cepheids and the right panel shows the combined LBT+M06 sample (N=122). The black contours represent the Z94-2 metallicity system, while the red contours are the B11-e system. The vertical blue lines mark the value of γ_1 found by M06. The solid contours are the 68% and 95% limits for two parameters, while the dashed contours are the limits obtained by imposing a prior on $\Delta\mu_{LMC}$, based on the Pietrzyński et al. (2013) eclipsing binary distance for the LMC and the maser distance of NGC 4258 from Humphreys et al. (2013).

LBT+M06 PDFs we find $\langle \Delta\bar{\mu}_{LMC} \rangle = 10.83 \pm 0.08_{stat} \pm 0.09_{sys}$. These values translate into LMC distances of 18.70 ± 0.12 and 18.57 ± 0.14. We choose to adopt the value from the combined LBT+M06 sample, which corresponds to an LMC distance of 51.82 ± 3.23 kpc (6% uncertainty). The smaller value of μ_{LMC} is driven by the stronger metallicity dependence found for the combined data. While it is trivial to derive the absolute PL relations from this distance, we provide a calibration in Table 11 for completeness. The uncertainty is dominated by the error on μ_{LMC}, yielding calibrations accurate to 13% in luminosity.

6.3 Summary

We have identified 81 Cepheids in the maser-host Galaxy NGC 4258 using data collected over 5 years from the LBT. Using image subtraction and empirical lightcurve templates, we were able to accurately phase the Cepheids, and we efficiently calibrated the Cepheid mean magnitudes using *HST*. Our final sample consists of 40 Cepheids, limited by the available *HST* data, with photometry in (up to) four different pass bands. Our sample was fit to PL relations determined from LMC Cepheids, using several models that explored uncertainty in the PL relations, the effects of extinction, the form of the extinction law, and metallicity on the determined distance modulus. Our key results are as follows:

(i) While the LBT data set does not support a statistically significant metallicity dependence, combining the LBT Cepheids with those from M06 yields a robust detection. The possible values of the observed effect are largely compatible with previously determined values from the literature, but uncertainties in the underlying metallicity scale make interpretation of the absolute effect difficult. We report a final value of $\gamma_1 = -0.61 \pm 0.21$ mag/dex, which uses the prevalent metallicity system of Zaritsky et al. (1994) and takes appropriate account of uncertainties in both the Cepheid mean magnitudes and the metallicity gradient of NGC 4258.

(ii) There is evidence for color corrections to the PL relations, which are consistent with either a grayer extinction law in NGC 4258 compared to the Milky way ($R_V = 4.9^{+0.9}_{-0.7}$), or a metallicity-dependent correction to the Cepheid mean magnitudes. While both effects are of physical interest, we lack sufficient 4 band photo-

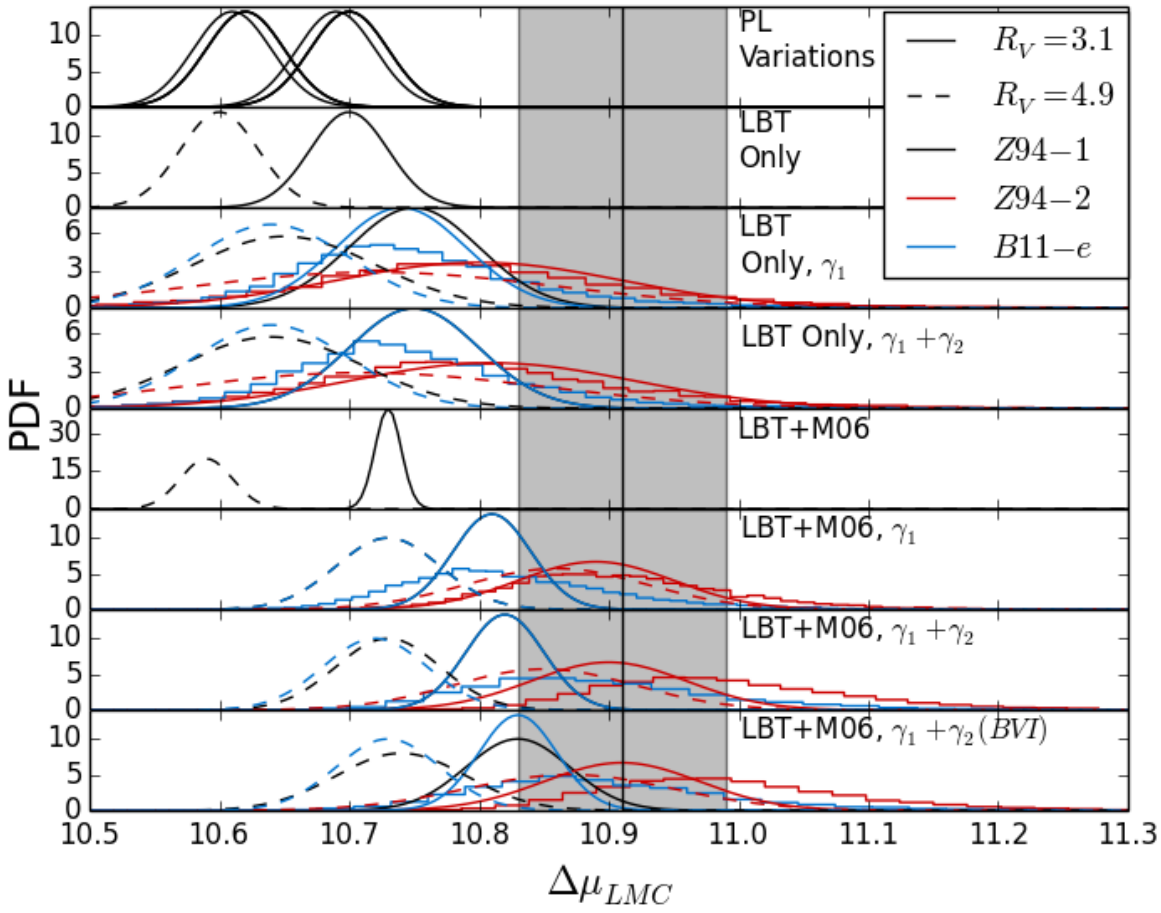

Figure 13. Probability distribution functions for $\Delta\mu_{LMC}$ from all models. The vertical black line marks the value of $\Delta\mu_{LMC} = 10.91 \pm 0.08$, based on the Pietrzyński et al. (2013) eclipsing binary distance for the LMC and maser distance of NGC 4258 (Humphreys et al. (2013)). The shaded gray region marks the 1σ uncertainty associated with this value.

metric data to disentangle these possibilities from other systematic effects.

(iii) Despite the degeneracy of the color corrections with a metallicity term, the data rule out the possibility that there is no metallicity effect at $\gtrsim 99\%$ confidence, as seen in the right-hand panel of Figure 10. Furthermore, incorporating a metallicity adjustment to the PL relations helps to reconcile our Cepheid distance with independent distances to the LMC and NGC 4258.

(iv) We report a final distance modulus between NGC 4258 and the LMC of $10.83 \pm 0.08_{stat} \pm 0.09_{sys}$ mag. Coupled with the maser distance from Humphreys et al. (2013), this implies that the LMC has a distance modulus of $\mu_{LMC} = 18.57 \pm 0.14$ mag (51.82 ± 3.23 kpc).

The LBT is an international collaboration among institutions in the United States, Italy and Germany. LBT Corporation partners are: The Ohio State University, and The Research Corporation, on behalf of The University of Notre Dame, University of Minnesota and University of Virginia; The University of Arizona on behalf of the Arizona university system; Istituto Nazionale di Astrofisica, Italy; LBT Beteiligungsgesellschaft, Germany, representing the Max-Planck Society, the Astrophysical Institute Potsdam, and Heidelberg University.

MMF thanks Kevin Croxall for helpful conversations about metallicity measurements and calibration issues. LMM & AGR acknowledge support by NASA through *HST* program GO-11570 from the Space Telescope Science Institute, which is operated by AURA, Inc., under NASA contract NAS 5-26555.

REFERENCES

Abazajian K. N., Adelman-McCarthy J. K., Agüeros M. A., Allam S. S., Allende Prieto C., An D., Anderson K. S. J., Anderson S. F., Annis J., Bahcall N. A., et al. 2009, ApJS, 182, 543

Alard C., Lupton R. H., 1998, ApJ, 503, 325

Anderson L., Aubourg É., Bailey S., Beutler F., Bhardwaj V., Blanton M., Bolton A. S., Brinkmann J., Brownstein J. R., Burden A., Chuang C.-H., Cuesta A. J., Dawson K. S., Eisenstein D. J., Escoffier S., Gunn J. E., Guo H., Ho S., Honscheid K., Howlett C., Kirkby D., Lupton R. H., Manera M., Maraston C., McBride C. K., Mena O., Montesano F., Nichol R. C., Nuza

S. E., Olmstead M. D., Padmanabhan N., Palanque-Delabrouille N., Parejko J., Percival W. J., Petitjean P., Prada F., Price-Whelan A. M., Reid B., Roe N. A., Ross A. J., Ross N. P., Sabiu C. G., Saito S., Samushia L., Sánchez A. G., Schlegel D. J., Schneider D. P., Scoccola C. G., Seo H.-J., Skibba R. A., Strauss M. A., Swanson M. E. C., Thomas D., Tinker J. L., Tojeiro R., Magaña M. V., Verde L., Wake D. A., Weaver B. A., Weinberg D. H., White M., Xu X., Yèche C., Zehavi I., Zhao G.-B., 2014, MNRAS, 441, 24

Bertin E., Arnouts S., 1996, A&AS, 117, 393

Bird J. C., Stanek K. Z., Prieto J. L., 2009, ApJ, 695, 874

Bonanos A. Z., Castro N., Macri L. M., Kudritzki R.-P., 2011, ApJ, 729, L9

Bono G., Caputo F., Fiorentino G., Marconi M., Musella I., 2008, ApJ, 684, 102

Bono G., Caputo F., Marconi M., Musella I., 2010, ApJ, 715, 277

Bresolin F., 2011, ApJ, 729, 56

Cardelli J. A., Clayton G. C., Mathis J. S., 1989, ApJ, 345, 245

Chavez J. M., Macri L. M., Pellerin A., 2012, AJ, 144, 113

Chiosi C., Wood P. R., Capitanio N., 1993, ApJS, 86, 541

De Marchi G., Panagia N., 2014, MNRAS, 445, 93

De Marchi G., Panagia N., Girardi L., 2014, MNRAS, 438, 513

Efstathiou G., 2014, MNRAS, 440, 1138

Flaherty K. M., Pipher J. L., Megeath S. T., Winston E. M., Gutermuth R. A., Muzerolle J., Allen L. E., Fazio G. G., 2007, ApJ, 663, 1069

Freedman W. L., Madore B. F., 2010, ARA&A, 48, 673

Freedman W. L., Madore B. F., 2011, ApJ, 734, 46

Freedman W. L., Madore B. F., Scowcroft V., Burns C., Monson A., Persson S. E., Seibert M., Rigby J., 2012, ApJ, 758, 24

Fukugita M., Ichikawa T., Gunn J. E., Doi M., Shimasaku K., Schneider D. P., 1996, AJ, 111, 1748

Gerke J. R., Kochanek C. S., Prieto J. L., Stanek K. Z., Macri L. M., 2011, ApJ, 743, 176

Gerke J. R., Kochanek C. S., Stanek K. Z., 2014, ArXiv e-prints

Giallongo E., Ragazzoni R., Grazian A., Baruffolo A., Beccari G., de Santis C., Diolaiti E., di Paola A., Farinato J., Fontana A., Gallozzi S., Gasparo F., Gentile G., Green R., Hill J., Kuhn O., Pasian F., Pedichini F., Radovich M., Salinari P., Smareglia R., Speziali R., Testa V., Thompson D., Vernet E., Wagner R. M., 2008, A&A, 482, 349

Gordon K. D., Clayton G. C., Misselt K. A., Landolt A. U., Wolff M. J., 2003, ApJ, 594, 279

Gould A., 1994, ApJ, 426, 542

Harris J., Zaritsky D., 1999, AJ, 117, 2831

Hill J. M., Green R. F., Ashby D. S., Brynnel J. G., Cushing N. J., Little J., Slagle J. H., Wagner R. M., 2010, in Society of Photo-Optical Instrumentation Engineers (SPIE) Conference Series Vol. 7733 of Society of Photo-Optical Instrumentation Engineers (SPIE) Conference Series, The Large Binocular Telescope

Humphreys E. M. L., Reid M. J., Moran J. M., Greenhill L. J., Argon A. L., 2013, ApJ, 775, 13

Kanbur S. M., Ngeow C.-C., 2004, MNRAS, 350, 962

Kelly B. C., 2007, ApJ, 665, 1489

Kennicutt Jr. R. C., Stetson P. B., Saha A., Kelson D., Rawson D. M., Sakai S., Madore B. F., Mould J. R., Freedman W. L., Bresolin F., Ferrarese L., Ford H., Gibson B. K., Graham J. A., Han M., Harding P., Hoessel J. G., Huchra J. P., Hughes S. M. G., Illingworth G. D., Macri L. M., Phelps R. L., Silbermann N. A., Turner A. M., Wood P. R., 1998, ApJ, 498, 181

Kewley L. J., Ellison S. L., 2008, ApJ, 681, 1183

Kochanek C. S., 1997, ApJ, 491, 13

Kuzio de Naray R., McGaugh S. S., de Blok W. J. G., 2004, MNRAS, 355, 887

Macri L. M., Calzetti D., Freedman W. L., Gibson B. K., Graham J. A., Huchra J. P., Hughes S. M. G., Madore B. F., Mould J. R., Persson S. E., Stetson P. B., 2001, ApJ, 549, 721

Macri L. M., Stanek K. Z., Bersier D., Greenhill L. J., Reid M. J., 2006, ApJ, 652, 1133

Mager V. A., Madore B. F., Freedman W. L., 2013, ApJ, 777, 79

Marconi M., Musella I., Fiorentino G., 2005, ApJ, 632, 590

Markwardt C. B., 2009, in Bohlender D. A., Durand D., Dowler P., eds, Astronomical Data Analysis Software and Systems XVIII Vol. 411 of Astronomical Society of the Pacific Conference Series, Non-linear Least-squares Fitting in IDL with MPFIT. p. 251

McGaugh S. S., 1991, ApJ, 380, 140

Mochejska B. J., Macri L. M., Sasselov D. D., Stanek K. Z., 2000, AJ, 120, 810

Ngeow C.-C., Kanbur S. M., Neilson H. R., Nanthakumar A., Buonaccorsi J., 2009, ApJ, 693, 691

Nishiyama S., Tamura M., Hatano H., Kato D., Tanabé T., Sugitani K., Nagata T., 2009, ApJ, 696, 1407

Pejcha O., Kochanek C. S., 2012, ApJ, 748, 107

Pellegrini E. W., Baldwin J. A., Ferland G. J., 2011, ApJ, 738, 34

Persson S. E., Madore B. F., Krzemiński W., Freedman W. L., Roth M., Murphy D. C., 2004, AJ, 128, 2239

Pietrzyński G., Graczyk D., Gieren W., Thompson I. B., Pilecki B., Udalski A., Soszyński I., Kozłowski S., Konorski P., Suchomska K., Bono G., Moroni P. G. P., Villanova S., Nardetto N., Bresolin F., Kudritzki R. P., Storm J., Gallenne A., Smolec R., Minniti D., Kubiak M., Szymański M. K., Poleski R., Wyrzykowski Ł., Ulaczyk K., Pietrukowicz P., Górski M., Karczmarek P., 2013, Nature, 495, 76

Pilyugin L. S., Thuan T. X., 2005, ApJ, 631, 231

Planck Collaboration Ade P. A. R., Aghanim N., Armitage-Caplan C., Arnaud M., Ashdown M., Atrio-Barandela F., Aumont J., Baccigalupi C., Banday A. J., et al. 2014, A&A, 571, A16

Riess A. G., Macri L., Casertano S., Lampeitl H., Ferguson H. C., Filippenko A. V., Jha S. W., Li W., Chornock R., 2011, ApJ, 730, 119

Riess A. G., Macri L., Casertano S., Sosey M., Lampeitl H., Ferguson H. C., Filippenko A. V., Jha S. W., Li W., Chornock R., Sarkar D., 2009, ApJ, 699, 539

Romaniello M., Primas F., Mottini M., Pedicelli S., Lemasle B., Bono G., François P., Groenewegen M. A. T., Laney C. D., 2008, A&A, 488, 731

Sandage A., Tammann G. A., Reindl B., 2004, A&A, 424, 43

Schlegel D. J., Finkbeiner D. P., Davis M., 1998, ApJ, 500, 525

Shappee B. J., Stanek K. Z., 2011, ApJ, 733, 124

Sirianni M., Jee M. J., Benítez N., Blakeslee J. P., Martel A. R., Meurer G., Clampin M., De Marchi G., Ford H. C., Gilliland R., Hartig G. F., Illingworth G. D., Mack J., McCann W. J., 2005, PASP, 117, 1049

Stanek K. Z., Udalski A., 1999, ArXiv Astrophysics e-prints

Stetson P. B., 1996, PASP, 108, 851

Subramanian S., Subramaniam A., 2013, A&A, 552, A144

Udalski A., Soszynski I., Szymanski M., Kubiak M., Pietrzynski G., Wozniak P., Zebrun K., 1999, Acta. Astr., 49, 223

van Albada G. D., 1980, A&A, 90, 123

Weiner B. J., Willmer C. N. A., Faber S. M., Harker J., Kassin S. A., Phillips A. C., Melbourne J., Metevier A. J., Vogt N. P., Koo D. C., 2006, ApJ, 653, 1049

Zaritsky D., Kennicutt Jr. R. C., Huchra J. P., 1994, ApJ, 420, 87

Table 1. NGC 4258 Cepheids

ID	Period	RA	Dec	$\hat{B}$	σ_B	$\hat{V}$	σ_V	$\hat{I}$	σ_I	$\hat{H}$	σ_H
1	23.75	184.84408	+47.22925	25.31	0.10	24.42	0.05	23.40	0.07	22.22	0.12
2	22.85	184.79454	+47.31188	25.24	0.19	24.40	0.12	23.17	0.13	...	...
3	84.59	184.68515	+47.28090	24.03	0.07	22.92	0.05	21.74	0.05	20.65	0.10
4	32.29	184.85758	+47.22968	25.60	0.07	24.52	0.06	23.44	0.10	22.30	0.10
5	24.38	184.73314	+47.27493	25.14	0.05	24.38	0.07	23.42	0.06	24.08	0.43
6	38.14	184.76166	+47.34665	25.48	0.24	23.98	0.08	22.82	0.09	...	...
7	31.29	184.80028	+47.20735	25.61	0.14	24.48	0.07	23.43	0.05	22.36	0.12
8	35.07	184.61344	+47.35845	24.76	0.30	23.65	0.11	22.76	0.07	...	...
9	38.78	184.72059	+47.39205	24.28	0.08	23.38	0.03	22.62	0.05	...	...
10	39.12	184.82310	+47.28103	24.90	0.10	23.92	0.05	23.06	0.09	...	...
11	16.87	184.77157	+47.22368	25.54	0.06	24.74	0.05	23.70	0.07	22.48	0.21
12	57.48	184.76648	+47.24888	24.03	0.07	22.93	0.09	21.89	0.08	21.05	0.13
13	23.26	184.71926	+47.25198	25.36	0.08	24.52	0.05	23.63	0.07	22.74	0.13
14	25.82	184.69883	+47.35581	24.91	0.05	24.07	0.03	23.29	0.07	22.24	0.20
15	39.90	184.73410	+47.40800	25.00	0.08	24.03	0.05	22.98	0.05	...	...
16	19.95	184.72128	+47.26102	25.32	0.09	24.43	0.06	23.34	0.07	22.47	0.18
17	33.89	184.87187	+47.22579	24.73	0.08	23.74	0.05	22.93	0.06	...	...
18	45.51	184.84633	+47.24654	24.30	0.05	23.42	0.04	22.52	0.06	...	...
19	33.58	184.71568	+47.24173	24.98	0.06	24.18	0.04	23.22	0.07	22.19	0.10
20	30.89	184.77245	+47.24221	25.52	0.12	24.48	0.05	23.47	0.07	22.55	0.12
21	18.45	184.68757	+47.33440	25.32	0.08	24.47	0.04	23.56	0.09	22.62	0.32
22	31.06	184.70008	+47.40291	24.99	0.11	24.05	0.06	23.06	0.08	...	...
23	39.06	184.73588	+47.39786	24.83	0.07	23.83	0.03	22.86	0.07	...	...
24	23.84	184.72887	+47.37800	25.30	0.07	24.27	0.06	23.21	0.07	22.19	0.15
25	26.99	184.69672	+47.33284	25.27	0.08	24.42	0.06	23.48	0.07	22.35	0.28
26	15.52	184.69183	+47.32215	25.60	0.08	24.73	0.05	23.82	0.07	23.30	0.29
27	21.17	184.76529	+47.22284	25.48	0.16	24.55	0.10	23.61	0.06	23.27	0.19
28	17.89	184.75834	+47.33870	25.76	0.08	24.90	0.05	23.97	0.08	...	...
29	26.83	184.74570	+47.25310	25.84	0.07	24.77	0.05	23.77	0.09	...	...
30	17.74	184.74875	+47.39152	25.48	0.09	24.82	0.07	24.07	0.09	...	...
31	36.95	184.71281	+47.35475	25.49	0.09	24.43	0.04	23.30	0.06	...	...
32	32.01	184.76900	+47.28149	25.66	0.12	24.93	0.11	23.47	0.07	23.79	0.20
33	60.98	184.69380	+47.27621	...	...	23.64	0.08	22.44	0.05	...	...
34	20.89	184.74066	+47.23927	25.91	0.08	24.92	0.05	23.66	0.09	22.14	0.15
35	24.59	184.85940	+47.24534	26.03	0.27	24.66	0.04	23.67	0.07	...	...
36	17.54	184.77167	+47.24397	25.29	0.07	24.49	0.03	23.79	0.08	22.56	0.18
37	36.44	184.75716	+47.22511	24.54	0.05	23.69	0.03	22.71	0.07	21.89	0.13
38	27.59	184.74555	+47.26070	25.35	0.07	24.27	0.04	23.05	0.10	25.40	0.39
39	36.67	184.71982	+47.31071	25.31	0.10	24.25	0.09	23.15	0.08	22.38	0.36
40	22.68	184.69844	+47.33315	25.23	0.10	24.40	0.06	23.52	0.07	22.58	0.36
41	19.84	184.70879	+47.43572	...	...	24.06	0.06	23.39	0.08	...	...
42	37.58	184.63776	+47.40795	24.84	0.09	23.86	0.04	22.96	0.05	...	...
43	44.65	184.61830	+47.40159	25.35	0.07	24.15	0.05	23.08	0.06	...	...

Periods, coordinates, and mean apparent magnitudes ($\hat{B}$, $\hat{V}$, $\hat{I}$, and $F160W$) of Cepheids identified with the LBT and calibrated with HST.

Table 2. NGC 4258 Cepheids (Unmatched)

ID	Period (days)	RA (degrees)	Dec (degrees)
44	32.26	184.62030	47.33033
45	42.80	184.73132	47.26414
46	17.43	184.77511	47.21588
47	47.49	184.65047	47.29608
48	22.09	184.78754	47.17365
49	53.31	184.65292	47.28472
50	25.10	184.85163	47.14524
51	33.19	184.85609	47.16104
52	16.53	184.76931	47.32193
53	15.04	184.73743	47.26392
54	17.86	184.76862	47.24926
55	33.22	184.71355	47.32232
56	16.99	184.83127	47.16879
57	18.84	184.66743	47.28373
58	17.72	184.73623	47.27552
59	89.52	184.70233	47.26043
60	13.40	184.77087	47.30534
61	16.80	184.68944	47.40506
62	26.30	184.71478	47.23186
63	61.73	184.80089	47.30431
64	46.93	184.71934	47.34864
65	28.04	184.72227	47.29616
66	44.27	184.74955	47.19773
67	14.48	184.85145	47.19703
68	14.15	184.66035	47.29288
69	48.19	184.73100	47.23930
70	28.26	184.64476	47.33938
71	18.75	184.70437	47.46564
72	16.82	184.60664	47.40835
73	14.30	184.51651	47.48418
74	19.28	184.61142	47.40765
75	34.50	184.60635	47.41172
76	21.70	184.66006	47.46426
77	12.75	184.47592	47.40205
78	43.02	184.64133	47.40476
79	56.71	184.60351	47.39328
80	29.82	184.44645	47.40800
81	17.40	184.62580	47.39856

Periods and coordinates for Cepheids with no identifiable match in HST images.

Table 3. Matched Cepheids

Cepheid (LBT ID)	LBT Period (Days)	P_{M06}-P_{LBT} (Days)	$B_{M06} - B_{LBT}$ (mag)	$V_{M06} - V_{LBT}$ (mag)	$I_{M06} - I_{LBT}$ (mag)
26	15.52	−0.23	−0.15	−0.07	0.02
21	18.45	−0.06	0.06	0.04	−0.02
40	22.68	0.11	0.00	−0.09	−0.10
14	25.82	−0.31	−0.05	−0.06	−0.18
25	26.99	1.25	0.04	−0.07	−0.09
39	36.67	0.03	−0.58	−0.43	−0.24
31	36.95	−2.06	−0.24	−0.22	−0.15
average		0.58	−0.13	−0.13	−0.11
σ		0.72	0.21	0.14	0.08

Comparison of periods and mean magnitudes for Cepheids found in common between this study and M06.

Table 4. PL Relations

Study	Band	a_F	σ_a	b_F	σ_b
OII	B	17.368	0.031	-2.439	0.046
	V	17.066	0.021	-2.779	0.031
	I	16.594	0.014	-2.979	0.021
N09	V	17.115	0.015	-2.769	0.023
	I	16.629	0.010	-2.961	0.015
	J	16.293	0.009	-3.115	0.014
	F160W	16.122	0.012	-3.182	0.019
	H	16.063	0.008	-3.206	0.013
P04	J	16.336	0.064	-3.153	0.051
	F160W	16.145	0.083	-3.213	0.066
	H	16.079	0.053	-3.234	0.042
($P > 10$ days)					
S04	B	17.136	0.177	-2.151	0.134
	V	16.906	0.135	-2.567	0.102
	I	16.456	0.111	-2.822	0.084
N09	V	17.122	0.195	-2.746	0.165
	I	16.440	0.132	-2.775	0.111
	J	16.075	0.139	-2.909	0.120
	F160W	15.895	0.179	-2.968	0.154
	H	15.832	0.113	-2.989	0.096

The OGLE II (Udalski et al. 1999, OII), Ngeow et al. (2009, N09), and Persson et al. (2004, P04) extinction corrected PL relations for the LMC, of the form $L_F(P) = a_F + b_F \log P$. PL relations for F160W were derived by linear interpolation of the J and H band coefficients, as a function of effective wavelength. Also included are the Sandage et al. (2004, S04) and N09 PL relations derived for long period Cepheids alone ($P > 10$ days).

Table 5. Extinction-only Distance Moduli

PL relations			$\Delta\mu_{LMC}$	χ^2/dof
OII BVI		P04 F160W	10.70 ± 0.03	1.00
OII BVI	N09 F160W		10.70 ± 0.03	1.01
OII BI	N09 V	P04 F160W	10.70 ± 0.03	1.09
OII BI	N09 V,F160W		10.69 ± 0.03	1.10
OII BV	N09 I	P04 F160W	10.62 ± 0.03	1.06
OII BV	N09 I,F160W		10.62 ± 0.03	1.05
OII B	N09 VI	P04 F160W	10.62 ± 0.03	1.02
OII B	N09 VI,F160W		10.61 ± 0.03	1.01
($P > 10$ days)				
S04BVI	N09 F160W		10.67 ± 0.03	1.04
S04B	N09 VI,F160W		10.60 ± 0.03	1.30

OII is OGLE II, Udalski et al. 1999, N09 is Ngeow et al. 2009, P04 is Persson et al. 2004, and S04 is Sandage et al. 2004.

Table 6. Radial Fits

Band	a	σ_a	b	σ_b
LBT Cepheids Only ($N = 40$)				
B	0.03	±0.04	-0.04	±0.05
V	0.00	±0.03	0.00	±0.03
I	-0.03	±0.05	0.03	±0.05
H	-0.09	±0.18	0.06	±0.20
LBT+M06 Cepheids ($N = 122$)				
B	0.02	±0.02	-0.04	±0.03
V	0.01	±0.01	-0.00	±0.02
I	-0.03	±0.01	0.05	±0.02
H	-0.11	±0.20	0.06	±0.22

Results of linear fits ($a + b(\rho_i/\rho_0)$) to the residuals from Model 1 as a function of galactocentric radius (see Figure 7).

Table 7. Metallicity Fits ($\gamma_1; \gamma_2 \equiv 0$)

Model	Gradient Slope	R_V	$\Delta\mu_{LMC}$	γ_1	χ^2/dof	μ_{LMC}
LBT Cepheids Only ($N = 40$)						
Standard	-0.49 ± 0.08	3.10	10.70 ± 0.03		1.00	18.70 ± 0.07
Extinction Law	-0.49 ± 0.08	4.90	10.60 ± 0.03		0.90	18.81 ± 0.07
Z94-1	-0.49 ± 0.08	3.10	10.75 ± 0.05	-0.18 ± 0.20	1.00	18.66 ± 0.08
Z94-2	-0.28 ± 0.04	3.10	10.80 ± 0.11	-0.32 ± 0.35	1.00	18.60 ± 0.13
B11-e	-0.18 ± 0.03	3.10	10.74 ± 0.05	-0.50 ± 0.54	1.00	18.66 ± 0.08
Z94-2 (boot)	-0.30 ± 0.05	3.10	10.79 ± 0.12	-0.29 ± 0.39		18.61 ± 0.13
B11-e (boot)	-0.19 ± 0.04	3.10	10.74 ± 0.09	-0.45 ± 0.62		18.66 ± 0.10
Z94-1	-0.49 ± 0.08	4.90	10.65 ± 0.07	-0.22 ± 0.25	0.91	18.76 ± 0.09
Z94-2	-0.28 ± 0.04	4.90	10.72 ± 0.14	-0.38 ± 0.43	0.91	18.69 ± 0.15
B11-e	-0.18 ± 0.03	4.90	10.64 ± 0.06	-0.59 ± 0.67	0.91	18.76 ± 0.09
Z94-2 (boot)	-0.30 ± 0.05	4.90	10.69 ± 0.14	-0.34 ± 0.42		18.71 ± 0.15
B11-e (boot)	-0.19 ± 0.04	4.90	10.64 ± 0.11	-0.54 ± 0.69		18.77 ± 0.11
LBT+M06 Cepheids ($N = 122$)						
Standard		3.10	10.73 ± 0.01		1.00	18.68 ± 0.07
Extinction Law		4.90	10.59 ± 0.02		0.91	18.82 ± 0.07
Z94-1	-0.49 ± 0.08	3.10	10.81 ± 0.03	-0.24 ± 0.08	0.97	18.59 ± 0.07
Z94-2	-0.28 ± 0.04	3.10	10.89 ± 0.06	-0.42 ± 0.14	0.97	18.52 ± 0.09
B11-e	-0.18 ± 0.03	3.10	10.81 ± 0.03	-0.65 ± 0.22	0.97	18.59 ± 0.07
Z94-2 (boot)	-0.30 ± 0.05	3.10	10.98 ± 0.10	-0.61 ± 0.21		18.43 ± 0.11
B11-e (boot)	-0.19 ± 0.04	3.10	10.88 ± 0.09	-0.95 ± 0.35		18.53 ± 0.11
Z94-1	-0.49 ± 0.08	4.90	10.73 ± 0.04	-0.40 ± 0.10	0.85	18.67 ± 0.08
Z94-2	-0.28 ± 0.04	4.90	10.86 ± 0.07	-0.71 ± 0.18	0.85	18.55 ± 0.10
B11-e	-0.18 ± 0.03	4.90	10.73 ± 0.04	-1.10 ± 0.28	0.85	18.68 ± 0.08
Z94-2 (boot)	-0.30 ± 0.05	4.90	10.94 ± 0.13	-0.89 ± 0.27		18.46 ± 0.14
B11-e (boot)	-0.19 ± 0.04	4.90	10.79 ± 0.13	-1.42 ± 0.45		18.61 ± 0.15

Table 8. Metallicity Fits [γ_1 & γ_2; $\boldsymbol{c} = \boldsymbol{p}_1$]

Model	Gradient Slope	R_V	$\Delta\mu_{LMC}$	γ_1	γ_2	χ^2/dof	μ_{LMC}
LBT Cepheids Only ($N = 40$)							
Z94-1	-0.49 ± 0.08	3.10	10.75 ± 0.05	0.00 ± 0.29	-0.29 ± 0.33	1.0	18.65 ± 0.08
Z94-2	-0.28 ± 0.04	3.10	10.81 ± 0.11	-0.14 ± 0.39	-0.28 ± 0.27	1.0	18.60 ± 0.13
B11-e	-0.18 ± 0.03	3.10	10.75 ± 0.05	0.02 ± 0.81	-0.80 ± 0.94	1.0	18.66 ± 0.08
Z94-2 (boot)	-0.30 ± 0.05	3.10	10.79 ± 0.12	-0.08 ± 0.59	-0.32 ± 0.60		18.61 ± 0.13
B11-e (boot)	-0.19 ± 0.04	3.10	10.74 ± 0.09	-0.20 ± 1.31	-0.44 ± 1.49		18.66 ± 0.10
Z94-1	-0.49 ± 0.08	4.90	10.64 ± 0.07	-0.56 ± 0.44	0.41 ± 0.44	0.91	18.76 ± 0.09
Z94-2	-0.28 ± 0.04	4.90	10.71 ± 0.14	-0.67 ± 0.53	0.34 ± 0.37	0.91	18.69 ± 0.15
B11-e	-0.18 ± 0.03	4.90	10.64 ± 0.06	-1.56 ± 1.24	1.16 ± 1.26	0.91	18.76 ± 0.09
Z94-2 (boot)	-0.30 ± 0.05	3.10	10.69 ± 0.14	-0.62 ± 0.89	0.31 ± 0.79		18.71 ± 0.15
B11-e (boot)	-0.19 ± 0.04	3.10	10.63 ± 0.10	-1.10 ± 2.01	0.62 ± 1.96		18.77 ± 0.11
LBT+M06 Cepheids ($N = 122$)							
Z94-1	-0.49 ± 0.08	3.10	10.82 ± 0.03	-0.00 ± 0.15	-0.44 ± 0.24	0.96	18.58 ± 0.07
Z94-2	-0.28 ± 0.04	3.10	10.90 ± 0.06	-0.20 ± 0.18	-0.44 ± 0.22	0.96	18.50 ± 0.09
B11-e	-0.18 ± 0.03	3.10	10.82 ± 0.03	0.02 ± 0.43	-1.23 ± 0.68	0.96	18.59 ± 0.07
Z94-2 (boot)	-0.30 ± 0.05	3.10	10.98 ± 0.10	-0.35 ± 0.26	-0.47 ± 0.24		18.42 ± 0.11
B11-e (boot)	-0.19 ± 0.04	3.10	10.88 ± 0.10	-0.43 ± 0.56	-0.95 ± 0.63		18.52 ± 0.11
Z94-1	-0.49 ± 0.08	4.90	10.73 ± 0.04	-0.61 ± 0.25	0.30 ± 0.33	0.85	18.68 ± 0.08
Z94-2	-0.28 ± 0.04	4.90	10.85 ± 0.07	-0.84 ± 0.26	0.22 ± 0.30	0.86	18.56 ± 0.10
B11-e	-0.18 ± 0.03	4.90	10.72 ± 0.04	-1.70 ± 0.71	0.87 ± 0.95	0.85	18.68 ± 0.08
Z94-2 (boot)	-0.30 ± 0.05	3.10	10.94 ± 0.13	-1.22 ± 0.40	0.44 ± 0.35		18.47 ± 0.14
B11-e (boot)	-0.19 ± 0.04	3.10	10.79 ± 0.13	-2.31 ± 1.00	1.17 ± 1.09		18.61 ± 0.15

Table 9. Metallicity Fits [γ_1 & γ_2; $\boldsymbol{c} = \boldsymbol{p}_{BVI}$]

Model	Gradient Slope	R_V	$\Delta\mu_{LMC}$	γ_1	γ_2	χ^2/dof	μ_{LMC}
LBT Cepheids Only ($N = 40$)							
Z94-1	-0.49 ± 0.08	3.10	10.76 ± 0.06	-0.65 ± 0.86	-0.26 ± 0.47	0.84	18.64 ± 0.09
Z94-2	-0.28 ± 0.04	3.10	10.82 ± 0.12	-0.84 ± 0.82	-0.29 ± 0.40	0.83	18.58 ± 0.14
B11-e	-0.18 ± 0.03	3.10	10.76 ± 0.06	-1.77 ± 2.46	-0.72 ± 1.33	0.84	18.65 ± 0.09
Z94-2 (boot)	-0.30 ± 0.05	3.10	10.80 ± 0.11	-0.82 ± 0.61	-0.29 ± 0.18		18.60 ± 0.13
B11-e (boot)	-0.19 ± 0.04	3.10	10.75 ± 0.07	-1.14 ± 1.49	-0.42 ± 0.60		18.65 ± 0.10
ZZ94-1	-0.49 ± 0.08	4.90	10.64 ± 0.07	0.02 ± 0.70	0.12 ± 0.28	0.73	18.77 ± 0.10
Z94-2	-0.28 ± 0.04	4.90	10.72 ± 0.16	-0.20 ± 0.74	0.10 ± 0.23	0.73	18.69 ± 0.17
B11-e	-0.18 ± 0.03	4.90	10.63 ± 0.07	0.09 ± 1.97	0.34 ± 0.79	0.73	18.77 ± 0.10
Z94-2 (boot)	-0.30 ± 0.05	3.10	10.69 ± 0.13	-0.12 ± 0.55	0.11 ± 0.11		18.71 ± 0.15
B11-e (boot)	-0.19 ± 0.04	3.10	10.62 ± 0.09	-0.08 ± 1.10	0.24 ± 0.29		18.78 ± 0.11
LBT+M06 Cepheids ($N = 122$)							
Z94-1	-0.49 ± 0.08	3.10	10.83 ± 0.04	-0.61 ± 0.33	-0.20 ± 0.18	0.9	18.57 ± 0.07
Z94-2	-0.28 ± 0.04	3.10	10.91 ± 0.06	-0.84 ± 0.35	-0.22 ± 0.19	0.9	18.49 ± 0.09
B11-e	-0.18 ± 0.03	3.10	10.83 ± 0.03	-1.69 ± 0.91	-0.56 ± 0.52	0.9	18.58 ± 0.07
Z94-2 (boot)	-0.30 ± 0.05	3.10	10.98 ± 0.09	-1.03 ± 0.37	-0.23 ± 0.13		18.42 ± 0.11
B11-e (boot)	-0.19 ± 0.04	3.10	10.88 ± 0.10	-1.87 ± 0.92	-0.50 ± 0.35		18.52 ± 0.11
Z94-1	-0.49 ± 0.08	4.90	10.74 ± 0.05	-0.14 ± 0.26	0.13 ± 0.11	0.79	18.66 ± 0.08
Z94-2	-0.28 ± 0.04	4.90	10.87 ± 0.08	-0.45 ± 0.30	0.13 ± 0.11	0.79	18.53 ± 0.10
B11-e	-0.18 ± 0.03	4.90	10.73 ± 0.04	-0.36 ± 0.73	0.36 ± 0.31	0.79	18.67 ± 0.08
Z94-2 (boot)	-0.30 ± 0.05	3.10	10.95 ± 0.13	-0.64 ± 0.35	0.13 ± 0.08		18.45 ± 0.15
B11-e (boot)	-0.19 ± 0.04	3.10	10.80 ± 0.14	-0.81 ± 0.77	0.30 ± 0.22		18.61 ± 0.15

Table 10. Bootstrapping Fits with Prior

Model	Gradient Slope	$\boldsymbol{c}$	$\Delta\mu_{LMC}$	γ_1	γ_2	μ_{LMC}
LBT Cepheids Only ($N = 40$)						
Z94-2 (boot)	-0.30 ± 0.05	$\boldsymbol{p}_1$	10.84 ± 0.07	-0.24 ± 0.47	-0.33 ± 0.61	18.56 ± 0.09
B11-e (boot)	-0.19 ± 0.04	$\boldsymbol{p}_1$	10.77 ± 0.08	-0.34 ± 1.18	-0.47 ± 1.52	18.63 ± 0.09
Z94-2 (boot)	-0.30 ± 0.05	$\boldsymbol{p}_{BVI}$	10.85 ± 0.06	-0.96 ± 0.50	-0.30 ± 0.18	18.55 ± 0.08
B11-e (boot)	-0.19 ± 0.04	$\boldsymbol{p}_{BVI}$	10.78 ± 0.07	-1.37 ± 1.58	-0.42 ± 0.63	18.62 ± 0.09
LBT+M06 Cepheids ($N = 122$)						
Z94-2 (boot)	-0.30 ± 0.05	$\boldsymbol{p}_1$	10.98 ± 0.09	-0.34 ± 0.25	-0.48 ± 0.24	18.43 ± 0.11
B11-e (boot)	-0.19 ± 0.04	$\boldsymbol{p}_1$	10.88 ± 0.09	-0.43 ± 0.54	-0.94 ± 0.63	18.52 ± 0.11
Z94-2 (boot)	-0.30 ± 0.05	$\boldsymbol{p}_{BVI}$	10.98 ± 0.09	-1.02 ± 0.37	-0.24 ± 0.13	18.42 ± 0.11
B11-e (boot)	-0.19 ± 0.04	$\boldsymbol{p}_{BVI}$	10.88 ± 0.09	-1.86 ± 0.92	-0.50 ± 0.35	18.52 ± 0.11

The prior imposed on $\Delta\mu_{LMC}$ is a gaussian with mean 10.91 and width 0.08, based on the Pietrzyński et al. (2013) eclipsing binary distance for the LMC and the maser distance of NGC 4258 from Humphreys et al. (2013). See the text for definitions of $\boldsymbol{c}$, $\boldsymbol{p}_1$, and $\boldsymbol{p}_{BVI}$. $R_V = 3.1$ for all of these models.

Table 11. Absolute PL relations

Study	Band	a	σ_a	b	σ_b
OII	B	-1.20	0.14	-2.439	0.046
	V	-1.50	0.14	-2.779	0.031
	I	-1.98	0.14	-2.979	0.021
P04	J	-2.23	0.14	-3.153	0.013
	F160W	-2.42	0.14	-3.213	0.013
	H	-2.49	0.14	-3.234	0.013

The calibrated optical OGLE II (OII, Udalski et al. 1999), and near-IR Persson et al. (2004, P04) PL relations, using $\mu_{LMC} = 18.57 \pm 0.14$. The PL relations are given in the form $L_F(P) = a_F + b_F \log P$.